




## Thermal vibrations in the inversion of dynamical electron scattering

Ziria Herdegen <sup>1</sup>, Benedikt Diederichs <sup>1,2</sup> and Knut Müller-Caspary <sup>1,\*</sup>

<sup>1</sup>*Department of Chemistry and Center for NanoScience, Ludwig-Maximilians-Universität München, Butenandstrasse 11, Munich, 81377, Germany*

<sup>2</sup>*Institute of Biological and Medical Imaging, Helmholtz Zentrum München, Neuherberg, 85764, Germany*



(Received 31 March 2024; revised 17 June 2024; accepted 18 July 2024; published 21 August 2024)

Relativistic forward scattering of electrons at finite temperature involves the incoherent superposition of diffraction patterns formed by different snapshots of thermal atomic displacements. In experiments, thermal vibrations lead to thermal diffuse scattering (TDS), partly dominating diffraction patterns of thick specimens. This study sheds light on the effects of TDS on solutions to the inverse scattering problem using combined real- and diffraction-space information acquired in a scanning transmission electron microscope (STEM) to retrieve the object's phase. Using frozen phonon multislice within the Einstein approximation, realistic ground truth data of 20-nm-thick SrTiO<sub>3</sub> is generated and subjected to contemporary inverse multislice schemes to retrieve the projected Coulomb potential slice-wise. We first classify phase retrieval algorithms as to their assumptions on periodicity along the incident beam direction, as well as pixelwise and parametrized reconstruction methods. It is found that pixelwise object reconstructions are capable of retrieving structural details qualitatively while being prone to contain TDS-related artifacts which can result in unphysical potentials. For pixelwise reconstructions of multiple independent specimen slices, we observe that the origin of TDS, i.e., thermal atomic displacements, starts to emerge naturally. However, the quantitative assessment tends to too small mean squared thermal displacements, also when reconstructing multiple object modes. Using an atomistically parametrized inversion strategy which exploits the explicit separation of thermal vibrations and potentials, temperature and chemistry of the specimen can be retrieved quantitatively with high accuracy.

DOI: [10.1103/PhysRevB.110.064102](https://doi.org/10.1103/PhysRevB.110.064102)

### I. INTRODUCTION

Having been a focus of x-ray science over decades, ptychography [1] evolved to a reliable technique for solving the inverse problem of electron scattering. One possibility to formulate the inversion as a tractable mathematical problem is to increase the dimensionality of the experimental data to induce redundancy. Thanks to the introduction of ultrafast diffraction cameras to scanning transmission electron microscopy (STEM) [2–6], comprehensive and densely sampled momentum space information can be recorded for each position of a scanning probe, i.e., an electron wave function which can be shaped and positioned flexibly by the optical system of the STEM. This combination of real- and diffraction-space information has enabled a plenitude of new methodologies to explore atomic-scale solid-state properties and to elucidate the physics of electron scattering, among them electron ptychography.

For example, scattering at thin specimens such as 2D materials or weakly scattering organic matter can be described

using single-scattering approaches [7]. Concerning the inverse problem, the complex object transmission function (OTF) can then be retrieved by both analytical direct schemes like the single-sideband method [8,9] or Wigner-distribution deconvolution [10], and by iterative ones, e.g., the extended ptychographical iterative engine (ePIE) [11]. Considering electron diffraction from the general perspective, however, introduces two major additional complications.

Firstly, multiple electron scattering becomes significant above specimen thicknesses of a few nanometres, limiting the applicability of single scattering approximations [12–14]. Forward scattering theories provide solutions to the dynamical electron diffraction problem in various frameworks, among them Bloch wave [15] calculations exploiting the periodicity of crystalline specimens, multislice [16] approaches without constraints as to translational symmetry, or scattering matrix approaches. Inversion strategies have recently been developed employing the scattering matrix concept [17–20], typically assuming periodic specimens to limit the matrix dimension to a computationally manageable size in practice. Importantly, inverse multislice has been introduced [21–25] which is not constrained to periodic specimens. To date, inverse multislice allows for structure determination with superresolution limited only by the thermal vibrations of the atoms [22].

Secondly, temperature effects lead to the breaking of any symmetries in the specimen and cause thermal diffuse scattering (TDS) which becomes partly dominant at elevated specimen thickness [26,27]. The TDS intensity governs the

\*Contact author: [k.mueller-caspary@cup.lmu.de](mailto:k.mueller-caspary@cup.lmu.de)

dark field in diffraction patterns and is sensitive to both, chemical composition and temperature [28–31]. Including TDS accurately in the inversion process is thus not only attractive from the application point of view, but also provides insights into the fundamental physics of electron scattering in dependence of the temperature. For scattering matrix approaches, TDS has successfully been included in forward simulations [32], whereas the introduction to inverse scattering beyond absorption potentials [33] is a remaining challenge. Contemporary inverse multislice schemes strive for finding the projected potentials of specimen slices as a static object to be determined such that consistency with experimentally recorded diffraction patterns is obtained. However, it is known from forward scattering theory that thermal effects involve the incoherent averaging over multiple states of the specimen, as included, e.g., in the frozen phonon (FP) model [34–36]. As a consequence there is not one, fix object to reconstruct, but an object which itself has never existed during experiments, formed from several snapshots of its thermal perturbations.

Contemporary inverse multislice methods have several possibilities to reproduce diffuse scattering.

(i) Inverse multislice exploiting the periodicity of crystalline specimens along the electron beam direction via reconstructing a single slice on a pixelated grid repeatedly used in the multislice simulation have pointed towards TDS be reconstructed only formally via introducing artifacts in the reconstructed potentials [25].

(ii) Optimizing multiple slice transmission functions of a specimen pixelwise offers sufficient freedom to produce diffuse scattering either in a fully coherent setup in unimodal manner for a single FP multislice configuration [22], or using a truly multimodal specimen setup [37], the latter reflecting the incoherent averaging within the FP concept.

(iii) Atomistically parametrized inversion has been suggested as a consequent inverse implementation of the FP multislice model [25], however, it has only been exploited for structure retrieval so far.

So far, pixelwise reconstructions using ansatz (ii) have successfully reconstructed different thermal displacement configurations within an ultrathin specimen of sub-nanometer thickness [37]. However, a quantitative evaluation of the mean squared displacements (MSDs) currently tends to underestimate thermal effects. Moreover, TDS causes significant fractions of the scattered intensity typically at elevated specimen thicknesses well beyond 10 nm. This suggests a systematic study on the quantification of MSDs assuming also thicker specimens with considerable amounts of TDS, and additionally the exploration of different regularization concepts. Parametrized strategies (iii) require substantial prior knowledge about the structure. Although the FP model is conceptually exactly represented there, distinguishing temperature effects from atomic number contrast remains a decisive task to measure temperature and chemistry quantitatively, because both tend to increase high-angle scattering in similar manner.

In this work, we briefly summarize the multislice concept first, together with the frozen phonon and Debye-Waller approach to account for temperature effects in scattering models (Sec. II). These forward models form the decisive kernel of inversion schemes and thus lay the basis for the subsequent

conceptual work. Section III provides an overview over different contemporary gradient-based inverse multislice concepts as a basis for the application in subsequent sections. This is followed by reconstructions of simulated momentum-resolved STEM data for an SrTiO<sub>3</sub> crystal in Sec. IV. Whereas structure retrieval has been the focus of previous work using parametrized inverse multislice [25], this study sheds light on the effect of thermal diffuse intensity in diffraction patterns on various inverse multislice reconstructions, of both pixelwise and parametrized nature. In particular, we analyze reconstructions obtained by pixelwise optimization of the OTF using ansatz (i) and (ii), being one computationally efficient model optimizing only one object transmission function used repetitively, but precluding the incorporation of TDS. Importantly, further models reconstructing each slice independently in uni- or multimodal manner are comprehensively studied, providing the opportunity of incorporating TDS for the multimodal setup. In this context we showcase the applicability of regularization techniques for pixelwise reconstructions [23,38,39], aiming at suppressing the generation of artifacts in individual slice transmission functions in favor of enforcing the solver to produce TDS by means of physically reliable MSDs. The findings are compared with an inverse algorithm featuring phonon ensemble averaging, drawing further attention to the quantitative reconstructions of atom potentials, which is a prerequisite for deciphering the accurate chemistry. In that respect, a comprehensive evaluation of the uniqueness of determining the type and MSD of an atom closes this section. Results are discussed in Sec. V, which furthermore includes a study on the decontamination of amorphous surface layers during the reconstruction by introducing a hybrid inverse multislice model which consists of both, atomistically parametrized and pixelwise reconstructed slice transmission functions.

## II. FORWARD SCATTERING THEORY

### A. Multislice concept

Forward momentum-resolved STEM simulations need to propagate an electron wave through the whole TEM, i.e., the probe-forming optics, the specimen and finally to the detector in the Fraunhofer diffraction plane. The incident electron probe wave function  $\Psi_{\text{in}}(\vec{r})$  can be obtained by an inverse Fourier transform of a complex pupil function, whose modulus is given by a binary aperture function  $A(\vec{k})$ . The vector  $\vec{k} = (k_x, k_y)$  denotes a reciprocal space coordinate, whereas  $k_{\text{max}}$  defines the radius of a circular aperture. Via  $|\vec{k}| = \sin(\theta)/\lambda$  spatial frequencies relate to angles  $\theta$  inclined with the optical axis, whereas  $\theta_{\text{conv}} = \arcsin(\lambda k_{\text{max}})$  defines the convergence semi-angle of the conical incident beam and  $\lambda$  the electron wavelength. Lens aberrations are included as a phase factor  $e^{-i\chi(\vec{k})}$  with  $\chi(\vec{k})$  the aberration polynomial, such that the probe wave function in real space reads

$$\Psi_{\text{in}}(\vec{r}, \vec{s}) = \mathcal{F}^{-1}[A(\vec{k}) \cdot e^{-i\chi(\vec{k})} \cdot e^{-2\pi i\vec{k} \cdot \vec{s}}], \quad (1)$$

with  $\vec{s}$  the scan coordinate. In this work, only a defocus  $a$  is considered such that  $\chi(k) = \pi \lambda a k^2$ .

Within the multislice scheme, multiple scattering is taken into account by the multiplication of the electron wave function with a complex OTF  $\Phi(\vec{r})$  in each slice, and Fresnel

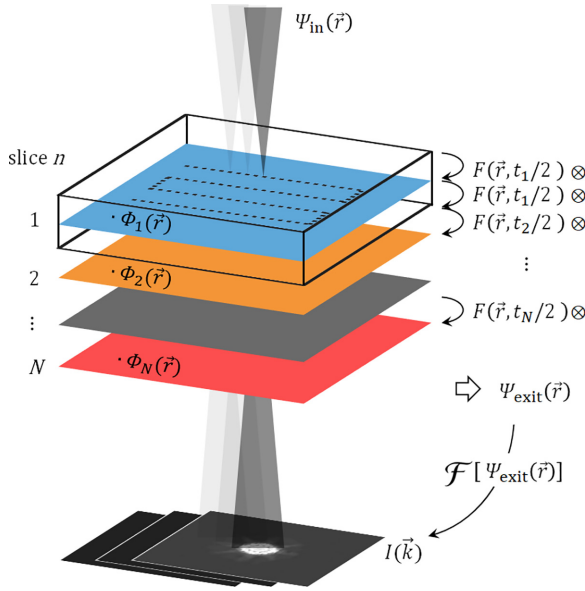


FIG. 1. Multislice algorithm scheme. The electron probe  $\Psi_{\text{in}}$  is propagated through the sliced specimen by alternating multiplication with the slice's object transmission function  $\Phi$  and convolution with the Fresnel propagator  $F$ . A Fourier transform of the exit wave  $\Psi_{\text{exit}}$  gives the diffraction patterns (DP).

propagation  $F$  in between. The OTF phase  $\varphi(\vec{r}) = \omega V_{\text{p}}(\vec{r})$  (phase grating) incorporates the interaction constant  $\omega$  and the projected slice potential

$$V_{\text{p}}(\vec{r}) = \int_{-\infty}^{\infty} \sum_m v_m(\vec{r} - \vec{r}_m, z) dz, \quad (2)$$

integrated along the beam direction  $z$ . A modulus of  $\Phi(\vec{r})$  can be used to account for absorption. In Eq. (2),  $v_m(\vec{r})$  is the Coulomb potential of atom  $m$  located at the origin,  $\vec{r}_m = (x_m, y_m)$  denotes its lateral position in the slice. As illustrated in Fig. 1, the exit wave function of a specimen with  $N$  slices is calculated as

$$\begin{aligned} \Psi_{\text{exit}}(\vec{r}, \vec{s}) &= F\left(\frac{1}{2}t_N\right) \otimes \Phi_N(\vec{r}) \cdot F\left(\frac{1}{2}t_N\right) \\ &\otimes F\left(\frac{1}{2}t_{N-1}\right) \otimes \Phi_{N-1}(\vec{r}) \cdot F\left(\frac{1}{2}t_{N-1}\right) \\ &\otimes \cdots \otimes F\left(\frac{1}{2}t_1\right) \otimes \Phi_1(\vec{r}) \cdot F\left(\frac{1}{2}t_1\right) \otimes \Psi_{\text{in}}(\vec{r}, \vec{s}), \end{aligned} \quad (3)$$

with  $\Phi_n$  the OTF of slice  $n$  having a thickness  $t_n$ . Note the Fresnel propagation over half the slice thickness so as to apply the OTF at the slice center. Furthermore, the first propagation of the probe  $\Psi_{\text{in}}$  can also be regarded as an additional defocus of the probe-forming lens, and the final propagation  $F(\frac{1}{2}t_N)$  to the exit face of the specimen is not observed in diffraction work, because it results in a phase plate in the back focal plane of the lens. Note that for the special case of equally thick slices with thickness  $t$ , Fresnel propagation in between the slices equals convolution with  $F(t)$ . After the last slice, the exit wave  $\Psi_{\text{exit}}(\vec{r}, \vec{s})$  is transferred to the farfield by Fourier transform, whereas the squared modulus gives the recorded diffraction pattern intensity at scan point  $\vec{s}$ ,

$$I(\vec{k}, \vec{s}) = |\mathcal{F}_{\vec{r}}[\Psi_{\text{exit}}(\vec{r}, \vec{s})](\vec{k})|^2. \quad (4)$$

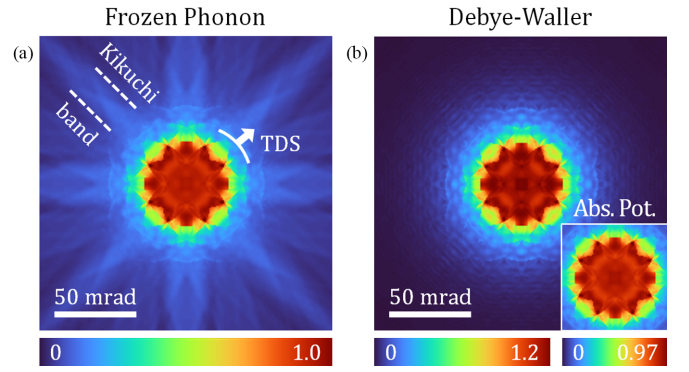


FIG. 2. Simulated position-averaged convergent beam electron diffraction (PACBED) patterns (square-root scale) using (a) frozen phonons in Einstein approximation and (b) the Debye-Waller damping. The inset in (b) shows the Ronchigram simulated with absorptive potentials. The intensities are normalized to the frozen phonon simulation.

Up to this point, the projected potentials are derived from the Coulomb potentials of static atoms, located at fixed positions over time. No temperature effect is included, such that inverting experimental momentum-resolved data based on Eq. (3) is incomplete.

## B. Frozen phonon model

The frozen phonon (FP) model provides a physically reliable incorporation of thermal diffuse scattering (TDS) by displacing atoms statistically from their equilibrium positions  $\vec{r}_m$ , and by averaging incoherently over the resulting diffraction patterns of multiple FP ensembles. The projected potential of a slice for one FP configuration  $\tau$  then reads

$$V_{\text{p}}^{\text{FP}}(\vec{r}, \tau) = \int_{-\infty}^{\infty} \sum_m v_m(\vec{r} - \vec{r}_m - \sqrt{\langle u_m^2 \rangle} \cdot \vec{g}_{m,\tau}, z) dz, \quad (5)$$

with two-dimensional Gaussian normal variables  $\vec{g}_{m,\tau}$  to describe the random displacement of atom  $m$  according to the atom's specific, temperature-dependent MSD  $\langle u_m^2 \rangle$  assuming the Einstein model. With Eq. (5) replacing Eq. (2), the multislice operation (3) yields a diffraction pattern  $I_{\tau}^{\text{FP}}(\vec{k}, \vec{s})$  with TDS from a single FP configuration  $\tau$  via Eq. (4). Note that  $V_{\text{p}}^{\text{FP}}(\vec{r}, \tau)$  does not obey the crystal symmetries anymore. Realistic diffraction patterns are obtained by averaging multiple FP configurations  $\tau = 1, 2, \dots, \mathcal{T}$ ,

$$I^{\text{FP}}(\vec{k}, \vec{s}) = \frac{1}{\mathcal{T}} \sum_{\tau=1}^{\mathcal{T}} I_{\tau}^{\text{FP}}(\vec{k}, \vec{s}). \quad (6)$$

Figure 2(a) shows a simulated position-averaged convergent beam electron diffraction (PACBED) pattern of an  $\text{SrTiO}_3$  crystal, generated using frozen phonons. The effect of TDS is clearly visible as diffuse intensity surrounding the Ronchigram, i.e., the bright field disk. It dominates the dark field and exhibits characteristic Kikuchi bands. While this model indeed offers a physically accurate solution to the problem for high-energy electrons and uncorrelated atomic vibrations, the computational demand increases proportionally to  $\mathcal{T}$ . Note

that the meanings of equilibrium atom positions  $\bar{r}_m$  and individual slice transmission functions  $\Phi_n$  cease as to modeling diffraction patterns including the dark field. Instead, a reconstruction based on the FP model is to yield a multimodal OTF ensemble  $\mathcal{T}$  for each slice.

### C. Debye-Waller approximation

The Debye-Waller (DW) model provides an efficient method in which the atomic potentials in Eq. (2) are replaced by their average over time to incorporate thermal vibrations. They are convolved with a Gaussian function, which is conveniently described in Fourier space by multiplying the atomic scattering amplitude  $f_m(\vec{k}) = \mathcal{F}[v_m](\vec{k})$  with the Debye-Waller factor

$$f_m^{\text{DW}}(\vec{k}) = e^{-\frac{1}{4}B_m k^2} f_m(\vec{k}). \quad (7)$$

Assuming isotropic thermal vibrations, the Debye parameter

$$B_m = 8\pi^2 \langle u_m^2 \rangle \quad (8)$$

is given by the MSD and can be found in literature for a variety of materials. For anisotropic vibrations,  $B_m$  is a second-rank tensor. Unlike the FP model, the DW approach retains the symmetry of the structure during simulations. Thus neither thermal diffuse intensity nor Kikuchi bands are generated as exemplified in Fig. 2(b). The neglect of TDS leads to too intense Bragg reflections which can be accounted for by adding an absorptive potential  $v_{m,\text{abs}}$  such that  $v_m \rightarrow v_m + i v_{m,\text{abs}}$  as was used to simulate the inset of Fig. 2(b). This converts  $\Phi_n(\vec{r})$  from a pure phase object to a slice transmission function with additional amplitude modulation dedicated to remove the TDS from the diffraction pattern [40–42]. Therefore care is to be taken when employing the DW scheme in an inverse model applied to diffraction patterns with TDS.

## III. INVERSE MULTISLICE PROBLEM

### A. Gradient-based optimization

The inverse problem, involving the reconstruction of an unknown specimen, essentially consists of iteratively performing forward simulations and optimizing the system's parameters until the simulated diffraction patterns closely match the experimental ones. The optimization parameters  $\{X\}$  may include characteristics of the specimen, such as the transmission functions  $\Phi_n$  of the individual slices, as well as electron probe parameters like aberrations or coherence. During the optimization a loss function  $\mathcal{L}_j$  is to be minimized, which calculates the error between the reconstructed and the experimental diffraction patterns in each epoch  $j$ . A convenient loss is defined as the mean absolute error

$$\begin{aligned} \mathcal{L}_j &= \frac{1}{N_{\text{pix}}} \sum_{\vec{k} \in \mathcal{K}} \sum_{\vec{s} \in \mathcal{S}} |I^{(X^{(j)})}(\vec{k}, \vec{s}) - I^{\text{exp}}(\vec{k}, \vec{s})| + \mu \mathcal{R}_j \\ &= \mathcal{L}_{1,j} + \mu \mathcal{R}_j \end{aligned} \quad (9)$$

involving the pixelwise subtraction of the diffraction patterns obtained by using the parameters  $\{X\}$  within the current forward model and the experimental ones, respectively. In Eq. (9),  $\mathcal{K}$  defines a region in diffraction space (i.e., solid angle range) to be used for calculating the loss,  $\mathcal{S}$  refers to

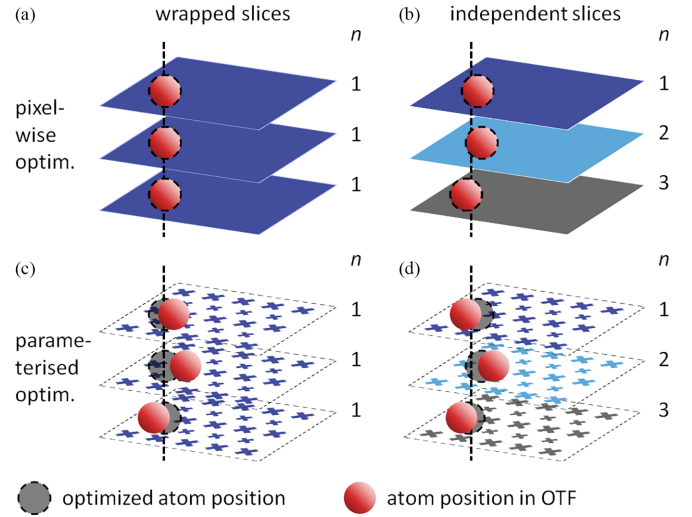


FIG. 3. Schematic illustration of the pixelwise [(a) and (b)] and parametrized [(c) and (d)] OTF optimization models. The atom positions received from the optimization are colored in grey and the atom peak positions in the OTF in red, which are equal in the pixelwise optimization model. Since in the parametrized model a FP simulation is included, the atom positions deviate from the optimized positions statistically according to the MSD.

a set of scan points  $\vec{s}$  to be taken into account, and  $N_{\text{pix}}$  is the total number of diffraction pattern pixels from which  $\mathcal{L}_1$  is determined. Optionally, a regularization term  $\mathcal{R}_j$  weighted by  $\mu$  can be added so as to prevent overfitting or promote desired properties of  $\{X\}$ , e.g., smoothness of  $\Phi_n$ .

The set  $\{X\}$  is adjusted in every epoch  $j$  along the negative loss gradient with respect to all parameters of interest, so as to minimize  $\mathcal{L}_{j+1}$ . For example, component  $l$  of  $\{X\}$  is updated via

$$X_l^{(j+1)} = X_l^{(j)} - \beta_l \cdot \frac{\partial \mathcal{L}_j}{\partial X_l^*} \quad (10)$$

with  $\beta_l$  the learning rate. Especially for inverse multislice within the FP approach, potentially accounting for partial coherence in addition, calculating the derivatives constitutes a computationally demanding task, for which, however, efficient backpropagation algorithms exist [43].

### B. Slicing concepts

It is clear that exploiting as much prior information as possible does not only accelerate the reconstructions due to, e.g., an educated guess of  $\{X^{(1)}\}$  but also reduces the risk of getting stuck in a local minimum of  $\mathcal{L}$ . Furthermore, the electron probe and slice transmission functions  $\Phi_n$  can either be represented as numerical, complex-valued arrays of independent pixels to form  $\{X\}$  with a huge cardinality of the order  $10^7$ , or be parametrized by a much sparser set of aberration coefficients and pre-calculated atomic potentials [44]. Together with the possibility to enforce periodicity of the specimen along electron beam direction or not, four different slicing concepts are possible as schematically illustrated in Fig. 3. Pixelwise strategies as shown in Figs. 3(a) and 3(b) offer enormous flexibility at individual pixel level to reconstruct slice

transmission functions  $\Phi_n$ . In the strict sense, solutions are not even bound to represent physically reliable OTF phases which correspond to projected potentials as in Eqs. (2), (5), and (7), but often resemble the atomic structure already well. In cases where the specimen is periodic in beam direction, a straightforward method to reduce both, computational effort and degrees of freedom, is to use the wrapped-slice scheme as in Fig. 3(a). This means optimizing the very same slice transmission function  $\Phi_1$  to be reused to describe the interaction in each slice. This model obviously precludes any ensemble averaging as required by Eq. (6) and is thus incapable of incorporating TDS correctly.

The situation is different in Fig. 3(b), where  $N$  independent slices are reconstructed. This allows for solutions nonperiodic in beam direction, being an interesting case as to study TDS. Let us assume the forward FP multislice case and a crystal having lattice periodicity along beam direction except for thermal disorder. Then Eq. (5) would be re-evaluated with the same equilibrium positions  $\vec{r}_m$  in each slice, however, with newly drawn random vectors  $\vec{g}_m$ . Thus a pixelwise reconstruction employing a specimen model as in Fig. 3(b) can, in principle, be expected to yield potential maxima at positions scattered around the equilibrium positions  $\vec{r}_m$  from slice to slice. Although first studies exist for multimodal reconstructions of a two-slice system [37], the quantitative nature of the obtained MSDs, retrieved potentials and the reconstruction settings pose further remaining challenges.

To constrain the OTF phases to be a sum of atomic potential functions, the specimen can be reconstructed parametrized [25], optimizing a set of specimen-characteristic parameters and recalculating the OTF from these in every iteration. The number of optimization parameters corresponds approximately to the number of atoms in the interaction volume. Making use of the so-released computing resources opens a way to incorporate a full FP model with  $\mathcal{T} = 1, \dots, 10$  into the reconstruction for a 50-slice system dealt with here, ensuring physically nearly correct inclusion of TDS and potential landscapes in accordance with self-consistent Hartree-Fock calculations yielding  $f_m(\vec{k})$  for isolated atoms [41,44,45]. Figure 3(c) exemplifies how TDS can be taken into account even within a wrapped-slice model for specimens periodic along the beam direction. Optimized are the atomic equilibrium positions  $\vec{r}_m$  and types via  $v_m$ , being common to all slices and FP configurations. However, random thermal displacements  $\sqrt{\langle u_m^2 \rangle} \cdot \vec{g}_{m,\tau}$  are added to  $\vec{r}_m$  every time the slice is used. Nonperiodic cases can be treated similarly, except that each slice exhibits an individual set of atom types and equilibrium positions, as depicted in Fig. 3(d).

At first sight, building the projected potential by atomic look-up tables implies all atomic types to be known beforehand. Moreover, the chemistry apparently remains static during the reconstruction because  $v_m(\vec{r})$  is not a differentiable parameter, in contrast to a pixelwise optimization of the OTF phase. As will be shown below, this problem can be addressed in two steps. Firstly, a pixelwise reconstruction is performed to identify atomic sites and guess atom types. Secondly, we employ a scalar, differentiable weighting parameter  $w$  for the atom potentials according to

$$v_m(\vec{r}) \longrightarrow w_m \cdot v_m(\vec{r}), \quad (11)$$

which replaces  $v_m$  in Eqs. (5) and (7), respectively. By this means, the derivative with respect to  $w_m$  indicates whether the scattering potential at site  $m$  is too high or too low, such that the atom type can be adjusted in the model for the next epoch. This strategy is used because the atomic potentials are discretized according to the periodic system. Note that by the incorporation of explicit atom types, and allowing for their update via a decision based on the weight gradient, mapping composition is in principle possible by ptychography. Since Z-contrast affects high angle scattering mostly, being in turn dominated by TDS, studying how accurate different inverse multislice concepts incorporate temperature effects and Z-contrast suggests itself and is dealt with next.

## IV. IMPACT OF TDS FOR DIFFERENT INVERSION CONCEPTS

### A. Ground truth simulation and reconstruction framework

Momentum-resolved STEM reference data of strontium titanate (SrTiO<sub>3</sub>) were simulated as the ground truth using the multislice algorithm as implemented in the TORCHSLICE [25] software employing the FP approximation with 25 thermal configurations newly drawn for each probe position and slice. In order to achieve a substantial amount of TDS, the specimen thickness was chosen to 50 unit cells, corresponding to approximately 20 nm. Electron beam incidence was along (100) with an energy of 80 keV. The slices had a constant thickness of one unit cell such that  $t = 0.3905$  nm, and real-space potentials have been sampled with a pixel size of 3 pm. Scattering factors for electrons from isolated atoms were taken from Lobato and van Dyck [44]. The electron probe was scanned across  $3 \times 3$  unit cells with a scan step size of 0.49 Å and a slight defocus of  $-5$  nm was used. Resulting CBEDs had a cutoff at  $1/6.1$  pm<sup>-1</sup> or 754 mrad, respectively. A part of the FP simulation is shown as a PACBED in Fig. 2(a). In the following, the slicing concepts introduced in Sec. III B are systematically studied as to the effect of TDS on the reconstruction, the prospects of regularization concepts and the capabilities to yield thermal MSDs and atomic types quantitatively.

For reconstructions the loss  $\mathcal{L}$  was calculated according to Eq. (9). The learning rate  $\beta$  was set to  $2 \times 10^{-3}$  for pixelwise reconstructions and to  $1 \times 10^{-2}$  for parametrized ones, and always halved when the loss increased. After 50 and 100 iterations the learning rate was reset to allow the escape from a local minimum. After 150 epochs at maximum, the loss was stable and the reconstruction terminated. In independent slice reconstructions, the slice sequence has been permuted several times during the reconstruction to minimize artifacts stemming from limited resolution along beam direction and limited surface sensitivity.

### B. Pixelwise reconstruction of a wrapped slice

#### 1. Incorporation of the full $\vec{k}$ space

Due to the lack of any ensemble averaging pointed out in Sec. III B, it is interesting to study how the pixelwise reconstruction of a wrapped slice accomplishes the loss minimization according to Eq. (9) when TDS is present as in Fig. 2(a). Two models for the slice transmission function  $\Phi_1$

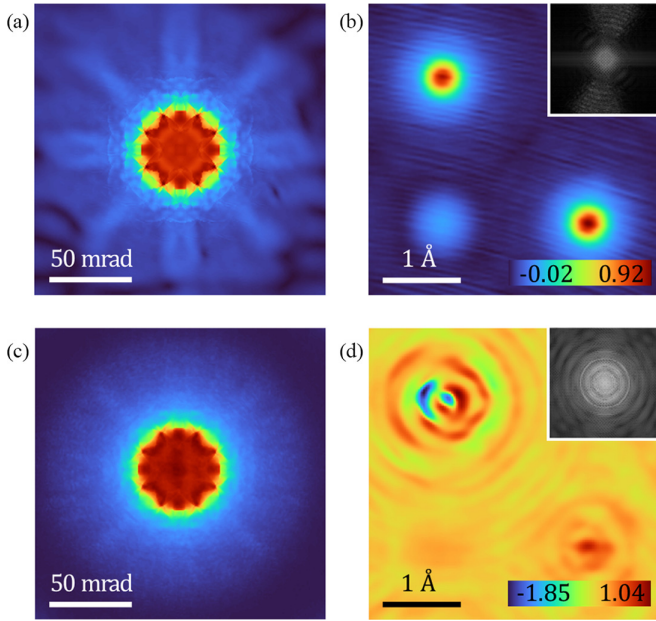


FIG. 4. Result of inverse multislice using a pixelwise reconstruction of a wrapped slice. (a) Simulated PACBED intensity (square root scale) using the reconstructed phase grating shown in (b) received by optimizing phase and amplitude of  $\Phi_1$ . (b) Section of the reconstructed phase grating (top left atom being Sr) in radian with log scaled FFT of the whole scan area as inset. FFT frequencies up to  $1 \text{ \AA}^{-1}$  [(c) and (d)] show the corresponding results for reconstructions optimizing a pure phase slice transmission function.

can be used. Either the slice transmission function is (i) a combined amplitude and phase object or (ii) a pure phase object. Considering the first case, optimizing a complex OTF  $\Phi_1$  for a slice thickness of 1 unit cell without any regularization leads to the data in Fig. 4, where Fig. 4(a) shows the PACBED simulated employing the reconstructed OTF whose phase is shown in Fig. 4(b). Furthermore, Figs. 4(c) and 4(d) exhibit the result of reconstructing a pure phase object. This reproduces the bright field part of the PACBED to some extent, but it is also obvious that the phase distribution in Fig. 4(d) does not resemble the atomic lattice very well. The following considerations as to the wrapped slice model thus refer to reconstruct both amplitude and phase of  $\Phi_1$ .

Regarding the summations in Eq. (9),  $\mathcal{K}$  span the whole diffraction space and  $\mathcal{S}$  the whole  $3 \times 3$  unit cells large scan region of the ground truth with equivalent super cell size as well as real and reciprocal space samplings, respectively. The PACBED in Fig. 4(a) exhibits diffuse intensity, reproducing also clearly visible bands surrounding the bright field disk. Given the static slicing model, the emulation of TDS features is surprising on the one hand. On the other hand, the striking similarity between Figs. 2(a) and 4(a) indicates that at least numerically, the pixelwise reconstruction possesses enough degrees of freedom so as to minimize Eq. (9) by matching model and ground truth diffraction patterns up to scattering angles of approximately  $4 \times \theta_{\text{conv}}$ . The origin becomes obvious in the reconstructed phase grating in Fig. 4(b), showing striplike artifacts superimposed to the atomic structure exemplarily depicted for a quarter of a unit cell. Although these

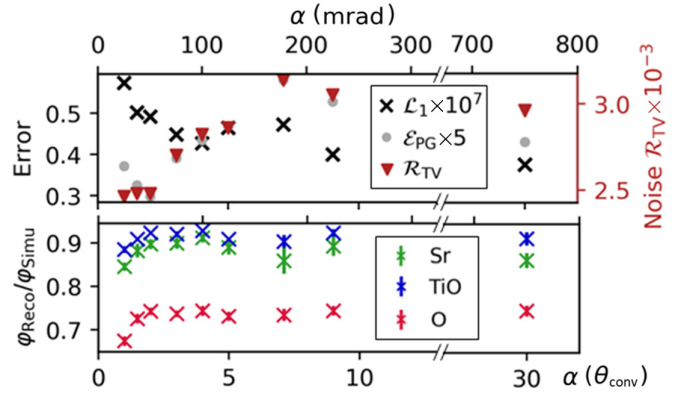


FIG. 5. Loss  $\mathcal{L}_1$ , PG-Error  $\mathcal{E}_{\text{PG}}$  and total variation  $\mathcal{R}_{\text{TV}}$  (top), and the relative maximum of atomic phases with STD (bottom) of pixelwise wrapped-slice reconstructions done using different reconstruction angles  $\alpha$ .

features provide a good recovery of the diffuse intensity distribution, no direct physical meaning can be assigned to them. Nevertheless, the efficiency of the wrapped slice approach is attractive in practice, which suggests exploring inverse multislice reconstruction conditions under which TDS-related artifacts can be suppressed as much as possible. To this end, adding a regularization term  $\mu\mathcal{R}$  in Eq. (9) is studied next.

## 2. Quantification of reconstruction errors

Figure 2 clearly indicates the difference between scattering models employing FP ensembles and the static case in Figs. 2(a) and 2(b), respectively. Because TDS dominates the diffraction space beyond 1-2 times the radius of the Ronchigram, which itself can be obtained rather accurately using the static DW model, a significant suppression of TDS-related artifacts is observed when  $\mathcal{L}_1$  is calculated from solid angles  $\mathcal{K}$  for which  $k \times \lambda < c \times \theta_{\text{conv}} =: \alpha$  with  $c > 1$  kept small, in favor of delivering smooth phase gratings with atomic potentials given by Eq. (7). Utilizing this relation, we propose suitable quantification of the diffuse intensity which is intrinsically produced to minimize  $\mathcal{L}_1$  and TDS-related phase artifacts. We define the total variation

$$\mathcal{R}_{\text{TV}} = \frac{1}{2N_{\text{pix}}} \sum_{i,j} (|\varphi_{i+1,j} - \varphi_{i,j}|^2 + |\varphi_{i,j+1} - \varphi_{i,j}|^2 + \varepsilon)^{\frac{1}{2}} \quad (12)$$

of the phase  $\varphi$  represented on a pixel array with  $N_{\text{pix}}$  pixels and  $(i, j)$  indexing a pixel. The parameter  $\varepsilon$  becomes relevant for regularization purposes below and is kept zero for the moment. The total variation is expected to increase with  $\alpha$ , which is indeed the case as shown by the triangles in Fig. 5. In particular,  $\mathcal{R}_{\text{TV}}(\alpha)$  stays small for  $\alpha \leq 2 \times \theta_{\text{conv}}$ , indicating that reconstructions with this setting are robust against TDS artifacts in the sense that atomically smooth OTF phases are obtained. For the present example,  $\mathcal{R}_{\text{TV}}$  stagnates for  $\alpha \geq 7 \times \theta_{\text{conv}}$ , presumably because the amount of TDS decreases with high scattering angles and thus causes no further significant artifacts in the reconstructed slice transmission function  $\Phi_1$ .

In addition, it is instructive to quantify the cumulative normalized differences between reconstruction and ground truth

as to the obtained phase gratings. To this end, we define

$$\mathcal{E}_{\text{PG}} = \sum_{\vec{r}} \frac{|\varphi^{(X)}(\vec{r}) - \varphi^{\text{ref}}(\vec{r})|}{\sum_{\vec{r}} \varphi^{\text{ref}}(\vec{r})} \quad (13)$$

with  $\varphi^{(X)}$  and  $\varphi^{\text{ref}}$  being the phases of the final reconstruction and the ground truth, respectively and the sum over 1.5 unit cells.  $\varphi^{\text{ref}}$  has been derived using the DW model in Eq. (7), being equivalent to an ensemble average over Eq. (5). Since physics is invariant against a global constant phase shift, an offset was added to the phase of the reconstructions which minimized the error of the background being  $\varphi^{\text{ref}} < 0.1 \varphi_{\text{max}}^{\text{ref}}$  between the DW simulation and the reconstruction result. The error of the reconstructed diffraction patterns is quantified by the first summand  $\mathcal{L}_1$  of the loss in Eq. (9), multiplied by  $10^8$  for better presentation, if not stated differently.

As a matter of fact, subjecting increasing solid angles  $\mathcal{K}$  to the loss minimization lets the loss decrease with increasing  $\alpha$ , as illustrated by the black crosses in Fig. 5. Note that for scattering beyond the reconstruction angle  $\alpha$ , the intensity  $I^{(X)}(\vec{k})$  of the final reconstruction falls to zero, reducing the overall agreement. Conversely, the introduction of TDS-related artifacts to the reconstructed OTF increases the error of the phase gratings  $\mathcal{E}_{\text{PG}}(\alpha)$  as shown by the grey circles in Fig. 5, which follows the same trend as  $\mathcal{R}_{\text{TV}}(\alpha)$ . This confirms that the total variation is a reliable measure of the TDS-induced artifacts where  $\mathcal{E}_{\text{PG}}$  is in practice not available due to the insufficient knowledge of the ground truth. Additionally this suggests  $\mathcal{R}_{\text{TV}}$  to be an appropriate regularization term which is studied more extensively below.

So far, the considered error metric has statistical character. With respect to the sensitivity of inverse multislice to the local chemistry of the specimen, we add the ratio of the phase peaks within the reconstruction and ground truth, respectively in Fig. 5 for different atomic columns. In particular, an area of 4 unit cells has been considered, yielding several phase peaks for each of the different atomic columns containing Sr, TiO<sub>2</sub>, or O, from which mean and standard deviation have been determined. Although the accuracy increases up to a reconstruction angle of approximately  $\alpha = 2 \times \theta_{\text{conv}}$ , the obtained phases amount only to 90 and 70% of the true ones. This means that the reconstructed projected potentials tend to be underestimated significantly, a problem dealt with in more detail below.

### 3. Suppressing artifacts with regularization

The total variation  $\mathcal{R}_{\text{TV}}$  in Eq. (12) was shown to be a measure of the amount of TDS artifacts in reconstructions. Using the full diffraction space for the inverse problem becomes feasible, if smooth phase gratings are enforced via penalizing high-frequency noise in real space in terms of the regularization term in Eq. (9). To assure differentiability,  $\varepsilon = 10^{-8}$  is used for  $\mathcal{R}_{\text{TV}}$  regularizations in Eq. (12), and the impact  $\mu$  of the regularization term in Eq. (9) is systematically studied. Furthermore, we explore the performance of sparse frequency regularization

$$\mathcal{R}_{\text{SF}} = \frac{1}{N_{\text{pix}}} \sum_{\vec{k}} |\mathcal{F}[\Phi](\vec{k})|, \quad (14)$$

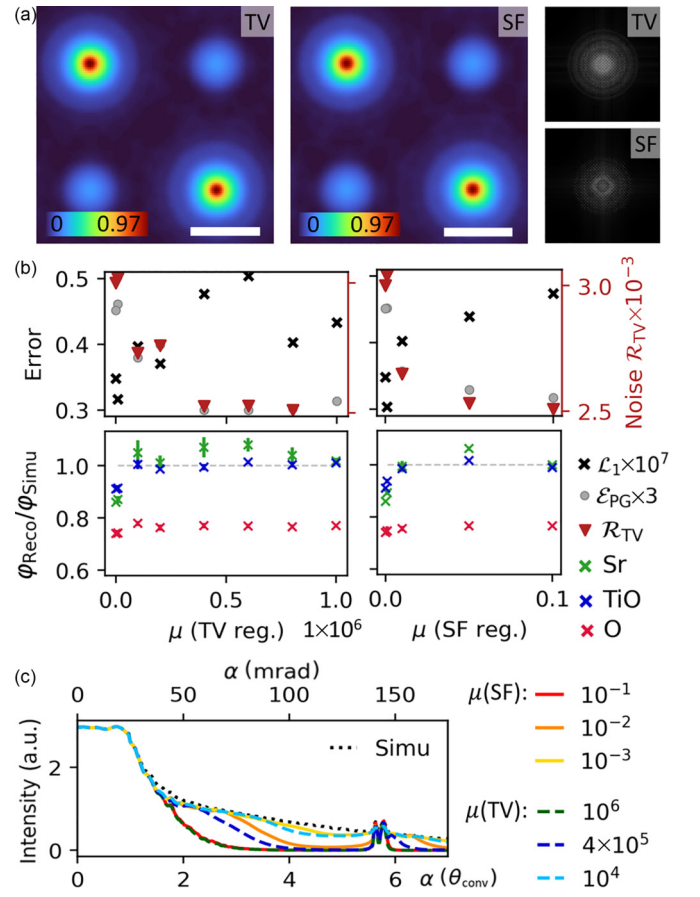


FIG. 6. Effect of total variation (TV) and sparse frequency (SF) regularization on pixelwise reconstructions of the single OTF within the wrapped-slice model. (a) 1 unit cell of the phase grating (top left atom being Sr) and FFTs of the whole scan area (right) of reconstructions using  $\mu = 10^6$  and  $\mu = 10^{-1}$  for TV and SF regularization, respectively. Phase grating scale bars, 1 Å. FFTs are in log scale up to  $1 \text{ \AA}^{-1}$ . (b) Losses  $\mathcal{L}_1$  and PG-errors  $\mathcal{E}_{\text{PG}}$  and the total variation  $\mathcal{R}_{\text{TV}}$  of the PG (top), and relative maximum atomic phases  $\varphi$  (bottom) of regularized reconstructions dependent on the regularization factor  $\mu$  for TV (left) and SF regularization (right). (c) Radial average of PACBEDs for selected regularization factors for both regularization methods, demonstrating the suppression of diffuse intensity as compared to the ground truth FP simulation (black dots).

which updates all Fourier coefficients towards zero with the same rate, such that small Fourier coefficients are suppressed more strongly in relative respect. Thus  $\mathcal{R}_{\text{SF}}$  steers the phase grating towards a sparse spectrum resulting in highly periodic reconstructions.

The reconstructions using  $\mathcal{R}_{\text{TV}}$  and  $\mathcal{R}_{\text{SF}}$  and their Fourier transforms are shown in Fig. 6(a), exhibiting a good suppression of the high-frequency phase artifacts caused by TDS for both regularization methods. It is to note that at the same time, the maximum phase is consistent with the nonregularized phase grating in Fig. 4(b). Although no solid angle  $\mathcal{K}$  needs to be restricted empirically, regularization comes along with the free choice of its strength  $\mu$  in Eq. (9). The parameter  $\mu$  has thus been varied from  $\mu = 0$  (no regularization) up to  $10^6$  or  $0.1$ , being strong regularizations for  $\mathcal{R}_{\text{TV}}$  and  $\mathcal{R}_{\text{SF}}$ , respectively.

As  $\mu$  increases, the total variation and thus the amount of TDS-related artifacts decreases. It then stagnates for both regularization schemes as depicted in Fig. 6(b). The same trend is observed for the error  $\mathcal{E}_{\text{PG}}$  of the reconstructed phase grating with respect to the DW expectation. The  $\mathcal{L}_1$  loss of the diffraction pattern increases significantly, indicating that the regularization terms indeed cause a strong suppression of the intensity scattered to high angles to favor smooth potentials, as intended. The ratio of the maximum reconstructed phases to those of the DW ground truth in Fig. 6(b) (bottom) yield a better agreement for the heavy atoms where a good match is obtained, but oxygen columns are still assigned too weak scattering of less than 80%. Characteristics of the reconstructed diffraction patterns are furthermore compacted in Fig. 6(c), where azimuthal PACBED averages are shown for various regularization strengths. The graphs confirm that reconstructions reproduce the diffraction pattern accurately within the central part dominated by Bragg scattering up to approximately  $1.5 \times \theta_{\text{conv}}$  and in the solid angle of the first Laue zone when using only small regularization strengths  $\mu$ , as seen by comparison with the FP ground truth (black dots). At the same time, both regularization methods,  $\mathcal{R}_{\text{TV}}$  and  $\mathcal{R}_{\text{SF}}$ , are capable of practically eliminating the occurrence of diffuse intensity if  $\mu$  set to high values.

As an intermediate conclusion, reusing the OTF in a pixelwise reconstruction can restore the atomic structure very well, but it is accompanied with artifacts when TDS is present in the dark field. Since the wrapped slices model does not allow for incorporating TDS, this slicing method has a limited sensitivity to characteristics of high-angle scattering during inversion of momentum-resolved STEM data, such as atomic number contrast due to local chemical composition gradients of the specimen. The oxygen columns are well differentiable from the Sr and the TiO columns in all cases, but their phase shifts are far smaller than the true ones.

### C. Slicewise optimization

Individual optimization of the slice OTFs as in Fig. 3(b) allows a symmetry break in  $z$  direction, and enables diffuse scattering either by a single snapshot of atomic displacements, or via multiple OTF modes according to true thermal diffuse scattering in FP approximation. Before addressing the inverse problem, let us frame the potential outcome in a forward simulation to eliminate, e.g., the impact of parameters inherent to the reconstruction such as loss definitions, learning rates or regularizations. To this end, Fig. 7 shows the losses of a DW simulation on the one hand, and FP simulations using different FP configurations on the other hand. The loss  $\mathcal{L}_1$  was calculated with respect to the ground truth simulations employing 10 to 100 FP configurations, and simulations have been performed for various specimen thicknesses. Each simulation was repeated 20 times and from this, the mean and the standard deviation of  $\mathcal{L}_1$  were calculated. The latter was found to be highest for 1 FP configuration and two unit cells specimen thickness and amounts to 2% of the loss, being negligibly small.

Regarding thicknesses below 100 unit cells (40 nm), Fig. 7 shows that a single FP snapshot results in a worse agreement with the ground truth than a DW simulation (horizontal

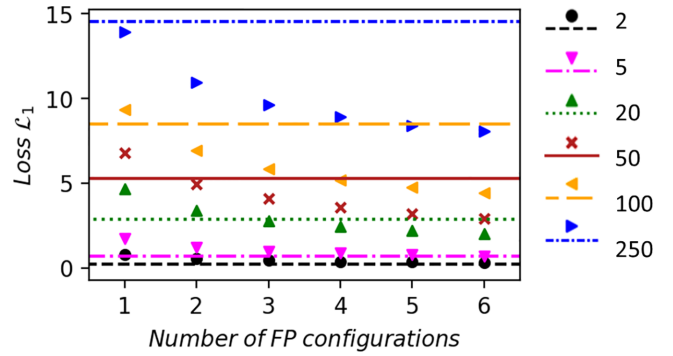


FIG. 7. Forward simulation study for various specimen thicknesses given in unit cells showing the losses to a full FP simulation for simulations using different numbers of FP configurations and for the respective DW simulation, represented by the lines.

lines) which lacks diffuse scattering entirely. Even for the high thickness of 250 unit cells (100 nm), diffuse intensity introduced by a single snapshot leads to an insignificantly better agreement. Note that  $\mathcal{L}_1$  has been calculated based on individual diffraction patterns, and that a single thermal snapshot is insufficient to represent TDS physically, since the simulation remains fully coherent. When dealing with a single FP configuration, we therefore only use the term *diffuse intensity* without the attribute *thermal*. Concerning thicknesses above 50 unit cells, at least two FP configurations are required to improve  $\mathcal{L}_1$  as compared to the DW model. For thinner specimens, the respective minimum number of FP configurations increases.

As to the reconstruction problem with TDS, this forward simulation study provides a gauge of how many object modes to allocate at least. In the present case of 50 unit cell thick SrTiO<sub>3</sub>, we concentrate on one to six object modes, as can be motivated as follows. Although one expects a single mode to cause higher  $\mathcal{L}_1$  than the DW approach, it might be an upper limit in some cases considering the capability of the computational resources. Thus it is tested in the following, to which extent structural disorder in the unimodally reconstructed phase gratings corresponds to the thermal MSDs of the ground truth. Note that the loss from the forward simulations in Fig. 7 does not allow direct conclusions on the quality of the reconstructed MSDs. Then, two object modes are considered since this is the minimum requirement for an FP implementation in the reconstruction. Six modes correspond to the maximum that can currently be considered with state-of-the-art hardware assuming the dimensionality of the problem considered here. In analogy to Sec. IV B, we consider two cases, where the slice transmission functions  $\Phi_{1\dots N}$  are either arbitrary complex or pure phase objects.

#### 1. Slices as amplitude and phase objects

*Unimodal reconstruction.* As to inverse multislice, Fig. 8(a) (left) shows the slice-averaged reconstructed phase grating received by optimizing 50 slice transmission functions independently pixelwise in amplitude and phase. The atomic landscape is clearly visible and the quantitative error to the ground truth, being  $\mathcal{E}_{\text{PG}} = 14.7$ , is slightly lower than those of the nonregularized wrapped-slices reconstruc-



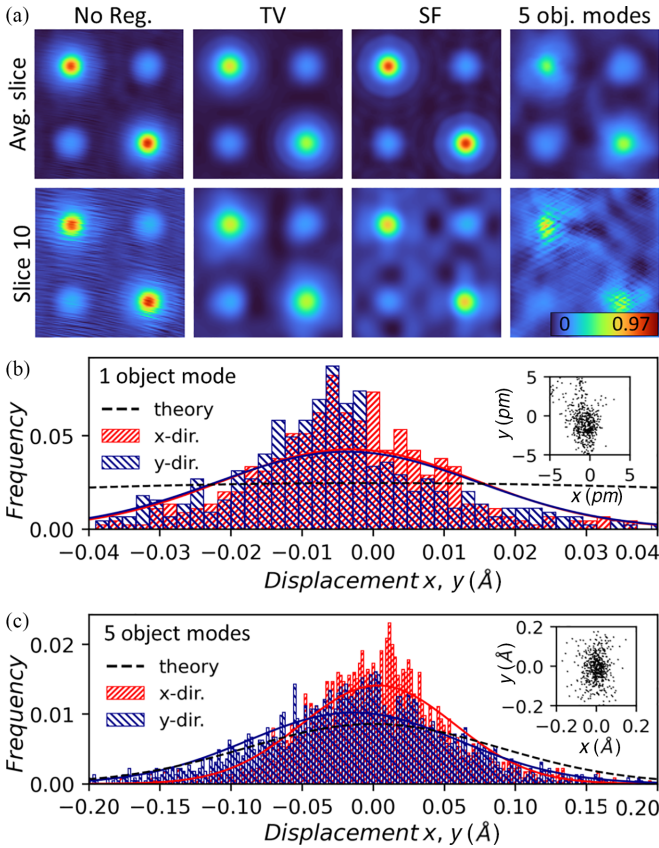


FIG. 8. Pixelwise reconstruction of independent slices optimizing phase and amplitude. (a) Averaged phase gratings and phase grating of slice 10 (top left atom being Sr) of pixelwise independent slice phase and amplitude reconstructions done without regularization (left), and with TV- and SF-regularization (middle) using the strengths  $\mu = 10^5$  and  $10^{-2}$ , respectively, and using 2 object modes (right). (b, c) Normalized atomic displacement distribution of the Sr columns with Gaussian fits of the reconstruction using independent slices and using 1 (b) and 5 (c) object modes. The inset shows the atomic displacement distribution in two dimensions.

tion. Although the averaged phase grating is relatively smooth ( $\mathcal{R}_{TV} = 1.08 \times \mathcal{R}_{TV, \text{simu.}}$ ), a closer look at the reconstructed phase distributions reveals that some individual layers are still affected by artifacts [Fig. 8(a), *no reg.*, *slice 10*]. With atomic phases being  $82 \pm 3\%$ ,  $87 \pm 3\%$ , and  $73 \pm 4\%$  of theory for Sr, TiO, and O, respectively, the reconstructed phase gratings do not show a significant improvement. However, the loss of  $\mathcal{L}_1 = 8.11$  is close to the loss of a simulation using 1 FP configuration in Fig. 7, suggesting a quantitative assessment of the potentially reconstructed thermal disorder.

Within an area of 4 unit cells, the centers of mass have been calculated in the reconstructed phase gratings inside patches around the average atom column position, whereas phases smaller than 5% than the maximum at the respective column were set to zero to suppress noise stemming from the reconstruction. We concentrate on the atomic columns consisting of pure elements, i.e., Sr and O. The spatial distribution of these site-specific centers of mass is shown in the inset of Fig. 8(b). The histogram of the atomic displacements in Fig. 8(b) indicates a decreasing frequency with increasing

TABLE I. Pixelwise optimization of 50 independent slice transmission functions optimizing phase and amplitude. Phase reconstruction errors  $\mathcal{E}_{PG}$  and reconstructed maximum atomic phases  $\varphi_{\text{Reco}}$  (normalized to the ground truth simulation) for the three different atom columns using no as well as TV and SF regularization and 1, 2, and 5 object modes (OM).

Reconstruction model	$\mathcal{E}_{PG}$ in %	$\varphi_{\text{Reco}}/\varphi_{\text{Simu}}$ in %		
		Sr	TiO	O
1 OM, no reg.	14.7	82 (3)	87 (3)	73 (4)
1 OM, $\mathcal{R}_{TV}$ , $\mu = 10^5$	19.5	57 (9)	49 (10)	68 (7)
1 OM, $\mathcal{R}_{SF}$ , $\mu = 10^{-2}$	12.7	83 (5)	85 (4)	77 (4)
2 OM, no reg.	21.8	78 (12)	75 (13)	66 (13)
5 OM, no reg.	36.3	45 (19)	49 (17)	63 (19)

thermal displacement, being physically reliable in general. However, the so-determined, averaged MSDs are 0.4 and 3.5  $\text{pm}^2$  for the Sr and O-columns. These are 0.6% and 5% of the theoretical values being 78.5 and 95.0  $\text{pm}^2$ , respectively. Note that atomicity and thermal effects have been found intrinsically by the pixelwise reconstruction which had been initialised by a flat OTF.

Although the atomic displacements observed in pixelwise optimized independent slices enable diffuse scattering, Fig. 8(a) demonstrates that the OTFs still show phase artifacts known from the wrapped slice approach. This supports the conclusion that this inversion scheme produces diffuse scattering in hybrid manner, via physically reliable but too small thermal displacements, and artificial phase noise in the OTFs to achieve consistency with the underlying experiment. Based on the regularization study in Sec. IV B where the phase noise could be suppressed successfully, exploring similar regularization concepts here suggests itself. In particular, favoring smooth scattering potentials while simultaneously allowing a single FP ensemble realized as a sequence of independently reconstructed slices, could be expected to push the inversion towards larger thus more accurate MSD. Importantly, using  $\mathcal{R}_{TV}$  and  $\mathcal{R}_{SF}$  regularizations both assure atomically smooth phases as shown in the middle of Fig. 8(a). Noting the identical color scaling, however, an underestimation of the phase maxima at all atomic sites is observed. Both regularization concepts even enhance the phase error  $\mathcal{E}_{PG}$  as summarized together with the relative atomic phases in Table I. With MSDs of 3.3 and 0.7  $\text{pm}^2$  for the Sr atoms and 4.2 and 1.0  $\text{pm}^2$  for the oxygen atoms, no significant improvement of the thermal displacements could be achieved. Using  $\mathcal{R}_{TV}$ , the obtained thermal displacements are in fact larger than those of the nonregularized results, but still amount to less than 5% of the theoretical values.  $\mathcal{R}_{SF}$  leads to even smaller displacements which is not surprising since promoting high periodicity and statistically displaced atoms contradict each other. Reasons for the algorithms getting stuck in a respective local minimum provoking too small atomic potentials and MSDs are elucidated in Sec. IV C.

*Multimodal reconstruction.* As shown in the simulation study in Fig. 7, using two object modes is expected to yield a better agreement of the diffraction patterns. When using two object modes, the loss decreased from 8.11 to 7.40. Increased

atomic displacements were observed, amounting 12 and 44 pm<sup>2</sup> (15% and 46% of theory) for the strontium- and oxygen columns, respectively. Using five object modes, a loss of 6.98 and a further broadening of the displacement distribution was found, as shown in Fig. 8(c). The measured displacements amount to 50 and 134 pm<sup>2</sup>, being 63% and 141% of the theoretical values. Table I shows the relative atomic potentials of the reconstructions which are still too low and decrease with the number of optimized object modes. Also some layers are still afflicted by artifacts as can be also seen in Fig. 8(a), going along with a high phase grating error  $\mathcal{E}_{PG} = 36.3\%$ .

## 2. Slices as pure phase objects

Recalling that the forward FP multislice concept involves slice transmission functions being pure phase objects in the absence of absorption, constraining the inverse model to functions  $\Phi_{1,\dots,N}$  with constant amplitude of one but varying phase becomes evident. Therefore the same inversion strategy as above has been used but only phases have been optimized.

*Unimodal reconstruction.* Figures 9(a)–9(f) show the unimodal result including different regularizations. The PACBED in Fig. 9(a) was simulated using the reconstructed phase gratings and, contrary to Fig. 4(c), also contains diffuse intensity similar to the ground truth in Fig. 2(a). The loss amounts to  $\mathcal{L}_1 = 9.5$ , being slightly higher than the error for the arbitrary complex slice transmission functions above. The lack of the amplitude degree of freedom paired with the reconstruction of the diffuse intensity implies the presence of structural disorder here. Indeed, the displacement statistics in Fig. 9(c) shows a Gaussian-shaped frequency distribution of the phase maxima from the atomic sites, however, being insignificantly broader than those for reconstructing both, phase and amplitude. Evaluated quantitatively, the MSDs take values of 2.3 and 8.1 pm<sup>2</sup> for Sr and O, respectively, being still less than 10% of the true values. High-frequency artifacts in between the atoms and the asymmetric distribution of the reconstructed projected atom potentials as shown in Fig. 9(b) can provide an alternative explanation for the emergence of the diffuse intensity. According to these unreasonable atomic phases and noticing the colorbar in Fig. 9(b), the phase error was determined to  $\mathcal{E}_{PG} = 49.9\%$ , being much higher than those of the other reconstructions carried out to this point.

According to Secs. IV B 3 and IV C 1, TV and SF regularization can suppress high-frequently phase artifacts, like also observed here. Both regularization methods lead to a smoother phase grating in between the atoms and also regarding the shapes of the atomic potentials as shown in Figs. 9(d), 9(e), which reduced the phase error to 12.8% and 19.0%, respectively. Restricting strong phase variations at the atomic sites again implies diffuse scattering being realized by atomic displacements which was the case for both regularization methods here. The statistical evaluation reveals MSDs of 32.4 and 50.7 pm<sup>2</sup> for Sr and O, respectively, being 95% and 65% of the theoretical values when using TV regularization. With SF-regularization MSDs of 8.0 and 20.6 pm<sup>2</sup> were received for Sr and O, being 10% and 26% of the theory. Although SF regularization provokes high periodicity and was shown to narrow the displacement distribution in Sec. IV C 1, the reconstruction shows rather large atomic displacements. In this case

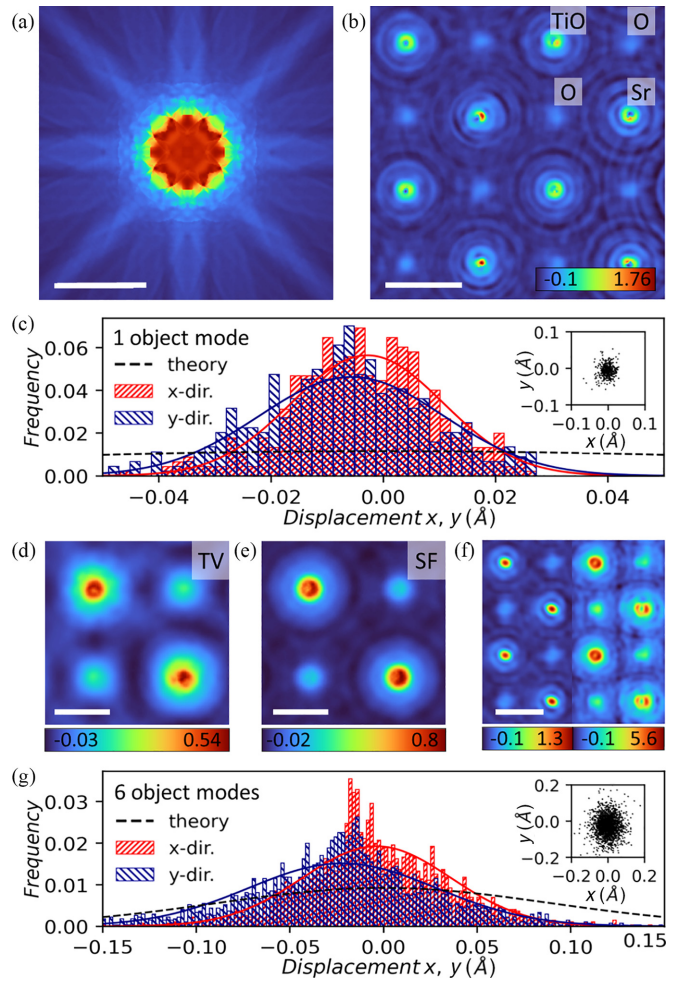


FIG. 9. Pixelwise reconstruction of independent slices with constant amplitude. (a) PACBED. Scale bar, 50 mrad. (b) Slice-averaged phase grating of the reconstruction. Scale bar, 2 Å. [(c) and (g)] Normalized atomic displacement distributions of the Sr columns of the reconstruction using independent slices with constant amplitude and (c) one or (g) six object modes, including Gaussian fits. The inset shows the atomic displacement distribution in two dimensions. [(d) and (e)] Slice-averaged phase gratings of reconstructions using TV and SF regularization (top left atom being Sr). Scale bar, 1 Å. (f) Phases (top left atom site being TiO) of slice 10 (left) and 9 (right) of the reconstruction using SF regularization. Scale bar, 2 Å.

the atomic phase maxima are found to be shifted collectively from their equilibrium position exemplarily shown for two different slices in Fig. 9(f). Due to asymmetric atomic potentials and regularization-induced modification of the atomic phases atomic reconstructions using pure phase object slice transmission functions could not improve the accuracy of quantitative atomic potentials. The maximum atomic phases of the respective reconstructions are summarized in Table II, together with the phase errors.

*Multimodal reconstruction.* Using two object modes, significantly increased MSDs were determined to 18 and 76 pm<sup>2</sup>, being 23% and 80% of the theoretical ones. The accuracy of the MSD measurements increased further when six object modes have been reconstructed, for which the displacement statistics is shown in Fig. 9(g). In this case, the MSDs amount

TABLE II. Pixelwise optimization of 50 independent pure phase-object slice transmission functions. Phase reconstruction errors  $\mathcal{E}_{\text{PG}}$  and reconstructed maximum atomic phases  $\varphi_{\text{Reco}}$  (normalized to the ground truth simulation) for the three different atom columns using no as well as TV- and SF- regularization and 1, 2, and 6 object modes (OM).

Reconstruction model	$\mathcal{E}_{\text{PG}}$ in %	$\varphi_{\text{Reco}}/\varphi_{\text{Simu}}$ in %		
		Sr	TiO	O
1 OM, no reg.	49.9	75 (10)	74 (8)	66 (11)
1 OM, $\mathcal{R}_{\text{TV}}, \mu = 10^5$	12.8	46 (19)	52 (23)	77 (36)
1 OM, $\mathcal{R}_{\text{SF}}, \mu = 10^{-2}$	19.0	71 (4)	76 (3)	108 (5)
2 OM, no reg.	40.8	78 (45)	59 (34)	119 (64)
6 OM, no reg.	24.7	87 (57)	78 (35)	110 (53)
6 OM, $\mathcal{R}_{\text{TV}}, \mu = 10^4$	32.5	59 (37)	51 (32)	86 (30)

to 20 and 95 pm<sup>2</sup> (25% and 100% of theory). Despite the enhancement of the accuracy of the atomic displacement measurement, the phase accuracy, i.e., the phase error and the height of the atomic phases did not improve, as compiled in Table II. Using TV-regularization, which showed a strong enlargement of the measured atomic displacements when using one object mode, MSDs of 61 and 142 pm<sup>2</sup> were found when using six object modes, which are 78% and 181% of the theoretical values. The phase error, however, increased to  $\mathcal{E}_{\text{PG}} = 32.5\%$  and the atomic potentials were found to be less accurate compared to the nonregularized reconstruction as shown in Table II. Since the overall phase accuracy decreased and the choice of the regularization strength leads to ambiguous results, we leave the derivation of potentially more reliable regularization strategies as a future task.

In summary, the emergent thermal disorder in independent slice reconstructions as a true physical effect is striking. Enabling the inclusion of incoherent scattering in the reconstruction model by optimizing multiple object modes promotes the formation of thermally displaced atomic ensembles, which can be improved for some cases by appropriate regularization techniques. Leaving the development of, e.g., regularization strategies to promote quantitatively reliable MSDs as a potential future challenge we now focus on parametrized approaches [25] to solve this task in the following.

#### D. Atomically parametrized reconstructions

Instead of trying to obtain the full potential landscape in Eq. (5) in pixelated manner, we now make use of the fact that the  $v_m(\vec{r})$ ,  $\vec{r}_m$  and MSDs  $\langle u_m^2 \rangle$  are known with sufficiently high accuracy to build an initial model. At first sight, reconstructing the ground truth with a very close model for the inversion appears trivial. On the contrary, it is by no means clear whether the inverse multislice which draws fully independent thermal snapshots as compared to the ground truth simulation, reproduces the true parameters and if so, how many FP configurations are necessary. From the practical point of view, pixelwise reconstructions as in the previous sections are preliminary steps, delivering appropriate structural guesses. Because we have seen that the pixelwise schemes tend to

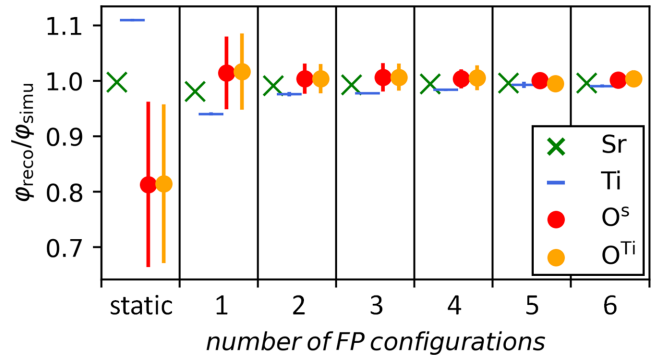


FIG. 10. Reconstructed weights (with standard deviation as error bar) of a parametrized reconstruction with wrapped slices using different numbers of FP configurations. In the first panel, the atom positions were assumed to be static, i.e., no atomic vibrations were allowed. O<sup>S</sup> denotes the single oxygen column and O<sup>Ti</sup> the oxygen in the TiO-column.

underestimate the potentials, the following parametrized reconstruction was initialized by a rather conservative guess with atomic weights  $w_m$  of 0.86, 0.91, and 0.74 for all Sr, Ti and O atoms according to Eq. (11). As the specimen is periodic in all three dimensions except for the thermal noise, wrapped OTF layers as in Fig. 3(c) were used.

#### 1. Number of phonon configurations during inversion

In a first study, the MSD were set to the true values, or set to zero and kept fix in both cases, whereas the weights  $w_m$  have been optimized using different numbers of FP ensembles. As shown in Fig. 10, increasing the number of phonon configurations in the inverse multislice leads to accurate potentials already for two thermal snapshots. The precision is finite only for the oxygen atoms and gets asymptotically better up to six FP configurations, the maximum considered in this study due to computational hardware limitations. This means that one to two FP ensembles suffice to correctly determine the Sr and Ti atomic types, whereas the light O atom can uniquely be identified as such from four to five thermal snapshots on. Note that the weight directly reflects the accuracy of the atomic phase maxima. Thus the phase of the oxygen atom columns, which have been initialized around 30% too low, now correspond to  $100 \pm 1\%$  of the ground truth. Disabling atomic vibrations in the reconstruction as indicated by the data labeled *static* in Fig. 10, the oxygen columns are assigned only 80%, titanium sites approximately 110% of the true potential, respectively.

#### 2. Optimizing thermal displacements

Since six FP configurations are found to yield a safely converged solution, corresponding final reconstruction results of the 4D-STEM data are compiled in Table III, together with those obtained from the pixelwise reconstruction models dealt with above. For the parametrized reconstructions, the losses of 2.93 and 6.79 match well with the losses of 2.95 and 6.80 estimated in the simulation study in Fig. 7 for six and one FP configurations. The reconstructions also show more than ten times lower PG errors as compared to the pixelwise methods. For the parametrized reconstructions, two optimization

TABLE III. Reconstruction losses  $\mathcal{L}_1$  ( $\times 10^8$ ), phase grating errors  $\mathcal{E}_{\text{PG}}$ , reconstructed relative maximum phases  $\varphi_{\text{Reco}}/\varphi_{\text{Simu}}$  for the three different atom columns and MSDs  $\sigma^2$  for the three atom species derived for different reconstruction methods: pixelwise using wrapped and independent slices each without (no reg.) and with TV/SF regularization and independent slices using multiple object modes (OM), parametrized reconstruction results using one and six FP configurations with the initial MSDs being fix and corresponding to the true values, and with the MSD being optimized and initialized as zero.  $\mathcal{E}_{\text{PG}}$ , and  $\varphi_{\text{Reco}}/\varphi_{\text{Simu}}$  are given in percent. The values in brackets are the standard deviation of  $\varphi_{\text{Reco}}/\varphi_{\text{Simu}}$  and the percentage of the measured MSDs to theory.

	$\mathcal{L}_1$	$\mathcal{E}_{\text{PG}}$	$\varphi_{\text{Reco}}/\varphi_{\text{Simu}}$			MSD $\sigma^2$		
			Sr	TiO	O	Sr	Ti	O
Pixelwise amplitude and phase								
Wrapped slice 50×								
No Reg.	3.48	15.0	85.9 (1.2)	90.9 (1.5)	739.7 (1.2)	–	–	–
$\mathcal{R}_{\text{TV}} \times 10^6$	4.33	10.3	101.9 (1.2)	101.1 (0.4)	77.4 (0.7)	–	–	–
$\mathcal{R}_{\text{SF}} \times 10^{-1}$	4.74	10.4	100.1 (0.3)	99.1 (0.03)	77.1 (0.5)	–	–	–
Pixelwise amplitude and phase								
50 independent slices								
1 OM, no reg.	8.11	14.7	82 (3)	87 (3)	73 (4)	0.4 pm <sup>2</sup> (0.6%)	–	3.5 pm <sup>2</sup> (3.7%)
1 OM, $\mathcal{R}_{\text{TV}} \times 10^5$	10.3	19.5	57 (9)	49 (10)	68 (7)	3.3 pm <sup>2</sup> (4.2%)	–	4.2 pm <sup>2</sup> (4.4%)
1 OM, $\mathcal{R}_{\text{SF}} \times 10^{-2}$	8.99	12.7	83 (5)	85 (4)	77 (4)	0.7 pm <sup>2</sup> (0.9%)	–	1.0 pm <sup>2</sup> (1.1%)
2 OM, no reg.	7.40	21.8	78 (12)	75 (13)	66 (13)	12 pm <sup>2</sup> (15%)	–	44 pm <sup>2</sup> (46%)
5 OM, no reg.	6.98	36.3	45 (19)	49 (17)	63 (19)	50 pm <sup>2</sup> (63%)	–	134 pm <sup>2</sup> (141%)
Pixelwise phase								
50 independent slices								
1 OM, no reg.	9.5	49.9	75 (10)	74 (8)	66 (11)	2.3 pm <sup>2</sup> (2.9%)	–	8.1 pm <sup>2</sup> (8.5%)
1 OM, $\mathcal{R}_{\text{TV}} \times 10^5$	7.27	12.8	46 (19)	52 (23)	77 (36)	32 pm <sup>2</sup> (41%)	–	41 pm <sup>2</sup> (43%)
1 OM, $\mathcal{R}_{\text{SF}} \times 10^{-2}$	5.36	19.0	71 (4)	76 (3)	108 (5)	8.0 pm <sup>2</sup> (10%)	–	21 pm <sup>2</sup> (22%)
2 OM, no reg.	8.5	40.8	78 (45)	59 (34)	119 (64)	18 pm <sup>2</sup> (23%)	–	76 pm <sup>2</sup> (80%)
6 OM, no reg.	7.2	24.7	87 (57)	78 (35)	110 (53)	20 pm <sup>2</sup> (25%)	–	95 pm <sup>2</sup> (100%)
6 OM, $\mathcal{R}_{\text{TV}} \times 10^4$	7.9	32.5	58.5 (37)	51.3 (32)	85.8 (30)	61 pm <sup>2</sup> (78%)	–	142 pm <sup>2</sup> (181%)
Parametrized atomic model								
6FP, MSD fix	2.93	1.65	99.6 (0.1)	100.5 (0.5)	99.6 (0.1)	79 pm <sup>2</sup> (100%)	56 pm <sup>2</sup> (100%)	95 pm <sup>2</sup> (100%)
6FP, MSD opt	2.89	1.49	99.6 (0.1)	99.5 (0.2)	98.0 (0.1)	71 pm <sup>2</sup> (90%)	55 pm <sup>2</sup> (99%)	75 pm <sup>2</sup> (79%)
1FP, MSD fix	6.79	1.82	98.1 (0.1)	103.5 (0.5)	97.7 (0.2)	79 pm <sup>2</sup> (100%)	56 pm <sup>2</sup> (100%)	95 pm <sup>2</sup> (100%)
1FP, MSD opt	6.22	4.88	98.9 (0.1)	97.0 (0.9)	93.3 (0.2)	42 pm <sup>2</sup> (53%)	42 pm <sup>2</sup> (75%)	31 pm <sup>2</sup> (33%)

settings are listed for the 6 FP and 1 FP case labeled *fix* and *opt*, respectively. The former denotes an inverse multislice initialized with the true MSD which was kept unchanged during the reconstruction, the latter corresponds to an initial setting of  $\langle u_m^2 \rangle = 0$  which was then optimized as well. In essence, this explores to which extent temperature and chemical contrast can be distinguished during inversion.

Setting the initial MSDs to zero and using only one FP configuration, the reconstructed MSDs of the Sr-, Ti- and O-displacements are 41.7, 41.6, and 30.9 pm<sup>2</sup> being 53%, 75%, and 33% of the true values. Averaging over six phonon ensembles, MSDs of 70.6, 55.0, and 74.8 pm<sup>2</sup> were received which are 90%, 99%, and 79% of the theoretical values. It becomes hence evident that increasing the number of FP ensembles improves also the accuracy of the displacement reconstructions. When leaving the MSD variable, a slightly reduced accuracy of the atomic weights, or equivalently, maximum phases is observed, and the error of the reconstructed phase is higher which is seen by comparing the *fix* and *opt* data in Table III. Note the availability of accurate MSD for Ti within the TiO column for the atomistically parametrized scheme. In theory, a reduction of the MSD increases the atomic potential in time average. Conversely a reduction of the weight decreases it.

In reconstructions, these two parameters seem to influence each other since lower MSDs correlate with lower maximum atomic phases or weights. Despite the reduced accuracy of the reconstruction when leaving the MSD variable, the loss was found to be smaller. A systematic investigation of how the atomic phases and the MSDs influence each other in the optimization process is elaborated in a simulation study presented next.

### 3. Sensitivity to atomic weights and mean square displacements

The pixelwise reconstruction of independent slices and the parametrized approach point towards taking a simultaneous determination of atom types and thermal displacements with care. Both impact high-angle scattering, motivating a systematic study of the uniqueness of determining the two parameters, atomic weight  $w_m$  and MSD  $\langle u_m^2 \rangle$ . To this end, a simulation series using 25 FP configurations was generated and the  $\mathcal{L}_1$  loss to the simulated ground truth has been calculated according to Eq. (9) in dependence of  $w_m$  and  $\sigma = \sqrt{\langle u_m^2 \rangle}$ .

Figure 11 shows loss maps for different probe positions on a regular grid over a quarter unit cell, with the corners of the grid lying on atom centers. The atomic column whose

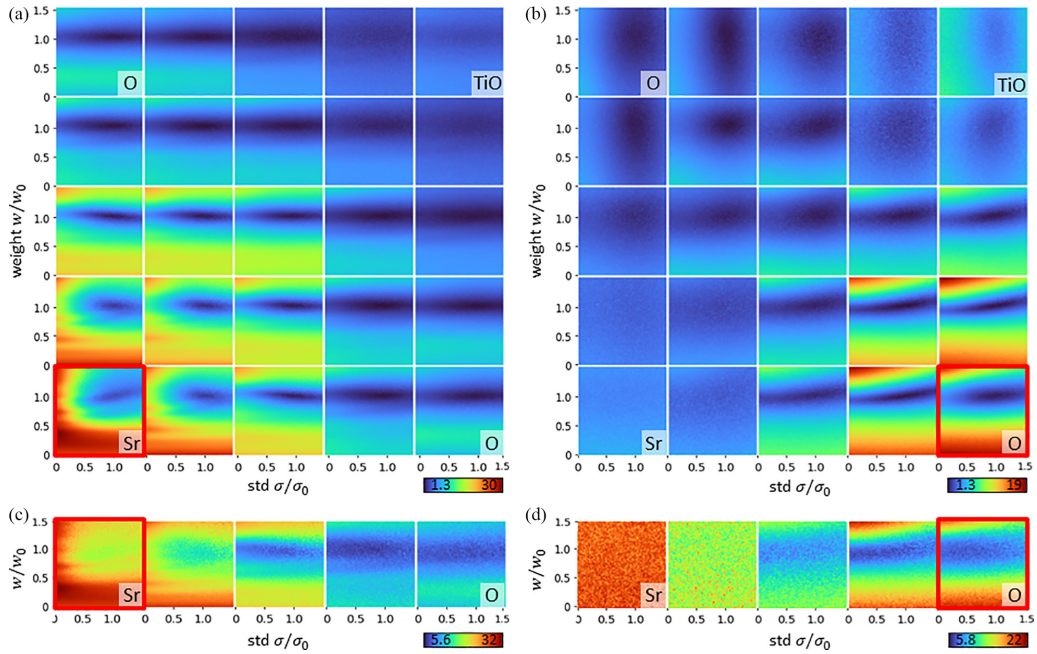


FIG. 11. Diffraction losses for various weights  $w$  and standard deviations  $\sigma$  of atomic displacements for different probe positions. In each map, the weight  $w$  and the STD  $\sigma$  of each atom are varied and 25 [(a) and (b)] or 1 [(c) and (d)] frozen phonon configurations are used. The probe is scanned over a quarter unit cell on a regular raster with the corners being on the given atom columns. (c) and (d) only show one row of the scan. Weights and standard deviations are given relative to their theoretical values  $w_0$  and  $\sigma_0$ .

weight and MSD were varied is framed in red, i.e., Fig. 11(a) depicts loss maps arranged on a scan grid while Sr parameters have been varied, in Fig. 11(b), the oxygen weight and MSD was varied at each of the  $5 \times 5$  scan positions. Instead of 25 FP configurations, only one thermal snapshot was used in Figs. 11(c) and 11(d). Note the parameter scaling relative to the ground truth, such that  $w/w_0 = 1$  and  $\sigma/\sigma_0 = 1$  reflect the correct setting, at which a deep loss minimum is expected in the ideal case. Regarding strontium properties, Fig. 11(a) exhibits loss minima at these ground truth values indeed. It moreover shows that within the  $3 \times 3$  scan points closest to the Sr site, loss gradients are large compared to the rest of the scan points depicting a shallow minimum. In other words, the gradients in Eq. (10) calculated with respect to  $w_{\text{Sr}}$  and  $\langle u_{\text{Sr}}^2 \rangle$  lead to significant strontium updates mostly based on diffraction patterns recorded at scan points close to Sr, as expected. Apart from that, a strong anisotropy of the loss is observed, favoring high sensitivity to the atomic weight  $w$ , but comparably low dependence on the MSD. For oxygen in Fig. 11(b), a fully analogous trend is observed, however, the sensitivity to atomic weight and MSD is confined to scan points close to the O column.

Conforming with strontium having a higher atomic potential than oxygen, the area around the atom providing weight information is higher for Sr, which still shows weight-sensitivity on the oxygen positions. Oxygen in contrast shows no weight dependency on the Sr column. For both atom species, a loss minimum is located around  $w/w_0 = 1$ , being most sensitive to the weight on and nearby the respective atom. In general the sensitivity of the 4D-STEM data to the oxygen parameters is lower, i.e., the difference between the highest and the lowest loss for the oxygen atom is 62% of the strontium loss range, for the probe being on the respective

atom center. This in combination with the smaller information radius around the atom can explain the higher error and lower accuracy of reconstructed oxygen parameters observed consistently throughout this study.

The effect of using fewer FP configurations is investigated in Figs. 11(c) and 11(d) where we find that the loss minimum broadens, corresponding to the weights being measurable less accurately if the number of phonon ensemble averages is reduced. This explains the observations made in Fig. 10 and the increase of MSDs with growing number of reconstructed object modes in pixelated reconstructions. Regarding the sensitivity of the loss to the atom's MSD, it is much lower than the weight dependency. Note that the position of the loss minimum is shifted to lower  $\sigma$  when using only one FP configuration for both atomic columns in Figs. 11(c) and 11(d), implying that using too few FP configurations during multislice inversion can lead to systematic errors.

Including a sufficient number of FP configurations is thus crucial for accurate quantitative reconstructions of both parameters simultaneously, atomic potentials and MSDs. Looking at the fine structure especially of the strontium-related losses in Fig. 11(a), several local minima occur which could favor the reconstruction of too low atomic weights  $w_m$  and MSDs  $\langle u_m^2 \rangle$ . Although the optimization pathways of the parametrized and pixelwise reconstruction (independent slices) cannot be compared directly, the partly too low potentials and MSDs found in Sec. IV C are probably related to this observation.

## V. DISCUSSION

Inversion of dynamical scattering has reached a level where statistical parameters arising from thermal motion of atoms

need to be included. This defines a hierarchy of models used during inversion. For crystals periodic in beam-direction the exploitation of the wrapped-slices model provides a computationally efficient method to retrieve the specimen's atomic lattice with limited sensitivity to the atomic potentials. Optimizing an amplitude and phase-object pixelwise, a high congruence of the diffraction patterns to the reference can be achieved formally, realized by high-frequency artifacts in the phase grating. Contrary, the use of a pure phase object cannot create diffuse intensity in the diffraction space, not even by introducing phase artifacts. This excludes the optimization of a pure phase object within the pixelwise wrapped-slice model for the reconstruction of strongly diffuse scattering specimen. When optimizing an amplitude and phase object using the full diffraction space including TDS, the atomic structure can be retrieved without artifacts by using appropriate regularization techniques. Therefore optimizing one wrapped amplitude- and phase slice transmission function in pixelwise manner is a reasonable approach to obtain a qualitative representation of the atomic structure, at least for the case considered here.

Enabling physically correct incorporation of temperature effects, the independent-slices model was shown to be able to detect thermal displacements conceptually as the root of TDS, being in agreement with recent literature on temperature effects in thin specimens [37]. This was found for both, optimizing slice transmission functions as amplitude and phase as well as a pure phase objects pixelwise. However, this study was not able to yield MSDs quantitatively via this approach since the diffuse scattering is produced in a hybrid manner by phase grating artifacts on the one hand and physically reliable but too small atomic displacements on the other hand. In particular, mixed amplitude and phase objects exhibited additional artificial phase noise, whereas pure phase objects lead to asymmetric phase distributions at the atomic sites. Using appropriate regularization techniques could increase the MSDs whereby TV regularization within a pure phase-object reconstruction retained the highest observed MSDs, amounting from 60% to 90% of the theoretical values. The lacking amplitude degree of freedom when assuming pure phase objects in combination with a regularization method aiming for physically more reliable atomic potentials appear to support TDS being realized by thermal atomic disorder. This, however, does not improve the reconstruction of atomic potentials quantitatively as the maximum atomic phases are still up to 50% too small. In fact, when expecting thermal displacements to be reconstructed correctly the atomic phases of the slices must be compared to the pure projected atom potentials and not to the time-averaged Debye-Waller potentials which are up to four times smaller for this simulation setting. Consequently, the quantitative information obtained from this model is rather poor. Moreover, reconstructing multiple object modes could enlarge the MSDs, with displacements increasing with the number of modes used. Nevertheless, this could not enhance the accuracy of the atomic potentials, presumably due to the high number of free parameters. Although this reconstruction model apparently considers thermal disorder in a physically true manner, the entanglement of TDS and atomic number contrast remains a substantial challenge.

Parametrizing the inverse scattering model can solve this problem as it explicitly discerns the atomic potential

distribution separated from thermal atomic movement. The increasing accuracy of the reconstructed atomic potentials with increasing numbers of FP configurations, as well as systematic errors, i.e., too small MSDs when using an insufficient number of phonon ensemble averages makes correct consideration of TDS within the model crucial for unique identification of atomic species. At present, the model assumptions still rely on idealizations which are, however, common also for forward simulations. In particular, considering thermal effects by means of the Einstein model neglects correlated atomic vibrations. In real experiments, these cause a faint substructure of TDS, which can already be accounted for by including second-neighbour interactions [46]. Thus including phonon dispersions beyond the Einstein model are a promising future perspective.

Besides TDS, inelastic scattering, especially due to plasmon excitations, has been found to cause significant redistributions of intensity in diffraction patterns [31,47–49]. A rigorous incorporation into the forward model involves the excitation and multislice propagation of a large set of mutually incoherent waves through the specimen volume for each scan point and thermal configuration. Given the present hardware capabilities, the direct implementation into gradient-based inverse multislice appears challenging for specimens with a reasonable number of slices. Instead, the inelastic scattering problem can be approximated by assuming commutativity of propagation and transition potential for the inelastic events. In this case, the effect of plasmon excitation as the most significant contribution can be accounted for by single (multiple) convolution of each diffraction pattern with a Lorentzian to account for single (multiple) plasmon excitations [48]. Including inelastic scattering as a Monte Carlo process into the conventional multislice run provides another option [49].

Considering real experimental data, counting noise might become relevant at low doses. For the reconstruction, replacing the  $\mathcal{L}_1$  loss in Eq. (9) by the Poisson loss [50] is recommended. Additionally, noise in the input data requires an estimate for the precision of the determined parameters, whereas the present work dealt with accuracy aspects only. Since error estimation within highly nonlinear, high-dimensional problems is nontrivial, precisions estimates might then be based on statistics over reference regions where the parameters can be assumed uniform.

In addition, atomistic parametrization suggests itself for crystalline specimens in the first place. Apart from that, also the study of crystalline materials often suffers from amorphous surface layers due to hydrocarbon contamination or preparation-induced damage. Consequently, setting up an initial atomistic structural model for the amorphous layers appears challenging. However, properties of interest concern the crystal in between, where the parametric model can be beneficial [25] as worked out here for thermal and chemical properties. In this respect, our methodology allows for hybrid models combining the different options in Fig. 3. In particular, a set of slices to be reconstructed pixelwise can be wrapped around the atomically parametrized ones. In a simulation study, we generated amorphous carbon layers of 5 nm thickness on the top and bottom face of 20-nm-thick

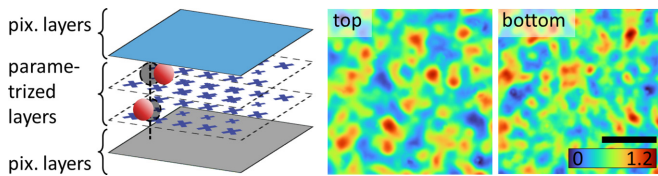


FIG. 12. Hybrid slice reconstruction model for consideration of contamination. Schematic illustration of a hybrid optimization layer system (left) and phase of pixelwise reconstructed 5-nm-thick amorphous carbon layers (right). The reconstructed data set was generated similar to this used in this work but with additional amorphous carbon layers on both sides of the specimen. Scale bar, 4 Å.

SrTiO<sub>3</sub>, and generated simulated diffraction patterns using FP multislice. As shown in Fig. 12, allocating two slices for pixelwise reconstruction at the top and bottom surface, respectively, could successfully decontaminate the specimen during reconstruction while yielding characteristic atom parameters of the crystalline part correctly, including TDS.

## VI. SUMMARY AND CONCLUSION

In this work, we systematically worked out the capabilities and the limitations of different inverse multislice strategies to retrieve specimen information comprising thermal vibrations and dynamical scattering. Pixelwise slice transmission function optimization methods resemble the atomic lattice well but are prone to include phase artifacts so as to achieve formal consistency with experimental diffraction patterns. Using

appropriate regularization terms could successfully suppress these artifacts. Optimizing 50 slice transmission functions individually yielded the diffuse CBED intensity very accurately by introducing thermal disorder to the atomic positions, which reflects the physical nature of TDS if multimodal objects are assumed. However, the quantitative evaluation of atomic potentials showed that these tend to be significantly too small. In contrast, a parametrized model restricts the slice transmission functions to a linear combination of projected atomic potentials, here obtained from Hartree-Fock calculations. Combined with the FP model, mean squared thermal displacements could be retrieved with almost 100% accuracy, while still exhibiting trustworthy chemical sensitivity.

To conclude, the introduction of inverse multislice opened the possibility to solve the inverse scattering problem for thick specimens. The omnipresence of thermal diffuse scattering needs to be viewed from two different directions. First, present pixelwise reconstruction methods need to be used carefully since they might be prone to artifacts, unless dedicated regularizations are used or further developed. Second, thermal diffuse scattering offers attractive perspectives to enhance the local chemical and temperature sensitivity in measurements providing combined real and momentum space data, if suitable inverse models are employed.

## ACKNOWLEDGMENTS

This work was supported by the Bavarian Hightech Agenda (Germany) within the EQAP grant and the Deutsche Forschungsgemeinschaft (DFG) under Grant No. EXC 2089/1 - 390776260 (Germany's Excellence Strategy).

- 
- [1] W. Hoppe, Beugung im inhomogenen Primärstrahlwellenfeld, I. Prinzip einer Phasenmessung von Elektronenbeugungsinterferenzen, *Acta Crystallogr., Sect. A* **25**, 495 (1969).
- [2] K. Müller, H. Ryll, I. Ordavo, S. Ihle, L. Strüder, K. Volz, J. Zweck, H. Soltau, and A. Rosenauer, Scanning transmission electron microscopy strain measurement from millisecond frames of a direct electron charge coupled device, *Appl. Phys. Lett.* **101**, 212110 (2012).
- [3] R. Plackett, I. Horswell, E. N. Gimenez, J. Marchal, D. Omar, and N. Tartoni, Merlin: a fast versatile readout system for Medipix3, *J. Instrum.* **8**, C01038 (2013).
- [4] K. Müller-Caspary, A. Oelsner, and P. Potapov, Two-dimensional strain mapping in semiconductors by nano-beam electron diffraction employing a delay-line detector, *Appl. Phys. Lett.* **107**, 072110 (2015).
- [5] M. W. Tate, P. Purohit, D. Chamberlain, K. X. Nguyen, R. Hovden, C. S. Chang, P. Deb, E. Turgut, J. T. Heron, D. G. Schlom, D. C. Ralph, G. D. Fuchs, K. S. Shanks, H. T. Philipp, D. A. Muller, and S. M. Gruner, High dynamic range pixel array detector for scanning transmission electron microscopy, *Microsc. Microanal.* **22**, 237 (2016).
- [6] D. Jannis, C. Hofer, C. Gao, X. Xie, A. Béch e, T. J. Pennycook, and J. Verbeeck, Event driven 4D stem acquisition with a timepix3 detector: Microsecond dwell time and faster scans for high precision and low dose applications, *Ultramicroscopy* **233**, 113423 (2022).
- [7] M. L. Leidl, C. Sachse, and K. Müller-Caspary, Dynamical scattering in ice-embedded proteins in conventional and scanning transmission electron microscopy, *IUCr* **10**, 475 (2023).
- [8] J. M. Rodenburg, B. C. McCallum, and P. D. Nellist, Experimental tests on double-resolution coherent imaging via STEM, *Ultramicroscopy* **48**, 304 (1993).
- [9] T. J. Pennycook, A. R. Lupini, H. Yang, M. F. Murfitt, L. Jones, and P. D. Nellist, Efficient phase contrast imaging in STEM using a pixelated detector. part 1: Experimental demonstration at atomic resolution, *Ultramicroscopy* **151**, 160 (2015); Special Issue: 80th Birthday of Harald Rose; PICO 2015–Third Conference on Frontiers of Aberration Corrected Electron Microscopy.
- [10] J. M. Rodenburg and R. H. T. Bates, The theory of super-resolution electron microscopy via Wigner-distribution deconvolution, *Philos. Trans. R. Soc. London, Ser. A* **339**, 521 (1992).
- [11] A. M. Maiden and J. M. Rodenburg, An improved Ptychographical phase retrieval algorithm for diffractive imaging, *Ultramicroscopy* **109**, 1256 (2009).
- [12] R. Close, Z. Chen, N. Shibata, and S. D. Findlay, Towards quantitative, atomic-resolution reconstruction of the electrostatic potential via differential phase contrast using electrons, *Ultramicroscopy* **159**, 124 (2015).

- [13] R. Hovden, H. L. Xin, and D. A. Muller, Channeling of a sub-angstrom electron beam in a crystal mapped to two-dimensional molecular orbitals, *Phys. Rev. B* **86**, 195415 (2012).
- [14] F. Winkler, J. Barthel, R. E. Dunin-Borkowski, and K. Müller-Caspary, Direct measurement of electrostatic potentials at the atomic scale: A conceptual comparison between electron holography and scanning transmission electron microscopy, *Ultramicroscopy* **210**, 112926 (2020).
- [15] H. Bethe, Theorie der Beugung von Elektronen an Kristallen, *Annalen der Physik* **392**, 55 (1928).
- [16] J. M. Cowley and A. F. Moodie, The scattering of electrons by atoms and crystals. I. A new theoretical approach, *Acta Crystallogr.* **10**, 609 (1957).
- [17] H. Brown, Z. Chen, M. Weyland, C. Ophus, J. Ciston, L. Allen, and S. Findlay, Structure retrieval at atomic resolution in the presence of multiple scattering of the electron probe, *Phys. Rev. Lett.* **121**, 266102 (2018).
- [18] P. M. Pelz, H. G. Brown, S. Stonemeyer, S. D. Findlay, A. Zettl, P. Ercius, Y. Zhang, J. Ciston, M. C. Scott, and C. Ophus, Phase-contrast imaging of multiply-scattering extended objects at atomic resolution by reconstruction of the scattering matrix, *Phys. Rev. Res.* **3**, 023159 (2021).
- [19] S. D. Findlay, H. G. Brown, P. M. Pelz, C. Ophus, J. Ciston, and L. J. Allen, Scattering matrix determination in crystalline materials from 4D scanning transmission electron microscopy at a single defocus value, *Microsc. Microanal.* **27**, 744 (2021).
- [20] J. J. Donatelli and J. C. H. Spence, Inversion of many-beam Bragg intensities for phasing by iterated projections: Removal of multiple scattering artifacts from diffraction data, *Phys. Rev. Lett.* **125**, 065502 (2020).
- [21] A. M. Maiden, M. J. Humphry, and J. M. Rodenburg, Ptychographic transmission microscopy in three dimensions using a multi-slice approach, *J. Opt. Soc. Am. A* **29**, 1606 (2012).
- [22] Z. Chen, Y. Jiang, Y.-T. Shao, M. E. Holtz, M. Odstrčil, M. Guizar-Sicairos, I. Hanke, S. Ganschow, D. G. Schlom, and D. A. Muller, Electron ptychography achieves atomic-resolution limits set by lattice vibrations, *Science* **372**, 826 (2021).
- [23] M. Schloz, T. C. Pekin, Z. Chen, W. Van den Broek, D. A. Muller, and C. T. Koch, Overcoming information reduced data and experimentally uncertain parameters in ptychography with regularized optimization, *Opt. Express* **28**, 28306 (2020).
- [24] A. Bangun, O. Melnykz, B. März, B. Diederichs, A. Clausen, D. Weber, F. Filbir, and K. Müller-Caspary, Inverse multislice ptychography by layer-wise optimisation and sparse matrix decomposition, *IEEE Trans. Comput. Imaging* **8**, 996 (2022).
- [25] B. Diederichs, Z. Herdegen, A. Strauch, F. Filbir, and K. Müller-Caspary, Exact inversion of partially coherent dynamical electron scattering for picometric structure retrieval, *Nat. Commun.* **15**, 101 (2024).
- [26] R. F. Loane, P. Xu, and J. Silcox, Thermal vibrations in convergent-beam electron diffraction, *Acta Crystallogr., Sect. A* **47**, 267 (1991).
- [27] Z. L. Wang, Dynamical inelastic scattering in high-energy electron diffraction and imaging: A new theoretical approach, *Phys. Rev. B* **41**, 12818 (1990).
- [28] P. D. Nellist and S. Pennycook, The Principles and Interpretation of Annular Dark-Field Z-Contrast Imaging, *Adv. Imag. Electron Phys.* **113**, 147 (2000).
- [29] A. Rosenauer, K. Gries, Knut Müller, A. Pretorius, M. Schowalter, A. Avramescu, K. Engl, and S. Lutgen, Measurement of specimen thickness and composition in  $\text{Al}_x\text{Ga}_{1-x}\text{N}/\text{GaN}$  using high-angle annular dark field images, *Ultramicroscopy* **109**, 1171 (2009).
- [30] J. M. LeBeau, S. D. Findlay, L. J. Allen, and S. Stemmer, Quantitative Atomic Resolution Scanning Transmission Electron Microscopy, *Phys. Rev. Lett.* **100**, 206101 (2008).
- [31] K. Müller-Caspary, O. Oppermann, T. Grieb, F. F. Krause, A. Rosenauer, M. Schowalter, T. Mehrtens, A. Beyer, K. Volz, and P. Potapov, Materials characterisation by angle-resolved scanning transmission electron microscopy, *Sci. Rep.* **6**, 37146 (2016).
- [32] S. D. Findlay, L. J. Allen, M. P. Oxley, and C. J. Rossouw, Lattice-resolution contrast from a focused coherent electron probe. Part II, *Ultramicroscopy* **96**, 65 (2003).
- [33] L. J. Allen, H. M. L. Faulkner, and H. Leeb, *Acta Cryst.* **A56**, 119 (2000).
- [34] D. Van Dyck, Is the frozen phonon model adequate to describe inelastic phonon scattering? *Ultramicroscopy* **109**, 677 (2009).
- [35] B. D. Forbes, A. V. Martin, S. D. Findlay, A. J. D'Alfonso, and L. J. Allen, Quantum mechanical model for phonon excitation in electron diffraction and imaging using a Born-Oppenheimer approximation, *Phys. Rev. B* **82**, 104103 (2010).
- [36] T. Niermann, Scattering of fast electrons by lattice vibrations, *Phys. Rev. B* **100**, 144305 (2019).
- [37] A. Gladyshev, B. Haas, T. M. Boland, P. Rez, and C. T. Koch, Reconstructing lattice vibrations of crystals with electron ptychography, *arXiv:2309.12017*.
- [38] P. Thibault and M. Guizar-Sicairos, Maximum-likelihood refinement for coherent diffractive imaging, *New J. Phys.* **14**, 063004 (2012).
- [39] W. Van den Broek and C. T. Koch, General framework for quantitative three-dimensional reconstruction from arbitrary detection geometries in tem, *Phys. Rev. B* **87**, 184108 (2013).
- [40] A. Weickenmeier and H. Kohl, Computation of absorptive form factors for high-energy electron diffraction, *Acta Crystallogr., Sect. A* **47**, 590 (1991).
- [41] A. L. Weickenmeier and H. Kohl, The Influence of Anisotropic Thermal Vibrations on Absorptive Form Factors for High-Energy Electron Diffraction, *Acta Crystallogr., Sect. A* **54**, 283 (1998).
- [42] D. M. Bird, Absorption in high-energy electron diffraction from non-centrosymmetric crystals, *Acta Crystallogr., Sect. A* **46**, 208 (1990).
- [43] W. Van den Broek and C. T. Koch, Method for retrieval of the three-dimensional object potential by inversion of dynamical electron scattering, *Phys. Rev. Lett.* **109**, 245502 (2012).
- [44] I. L. Hoyos and D. van dyck, An accurate parameterization for scattering factors, electron densities and electrostatic potentials for neutral atoms that obey all physical constraints, *Acta Crystallogr., Sect. A* **70**, 11 (2014).
- [45] P. A. Doyle and P. S. Turner, Relativistic Hartree-Fock X-ray and electron scattering factors, *Acta Crystallogr., Sect. A* **24**, 390 (1968).



- [46] D. A. Muller, B. Edwards, E. Kirkland, and J. Silcox, Simulation of thermal diffuse scattering including a detailed phonon dispersion curve, *Ultramicroscopy* **86**, 371 (2001).
- [47] A. Beyer, Florian F. Krause, Hoel L. Robert, S. Firoozabadi, T. Grieb, P. Kükelhahn, D. Heimes, M. Schowalter, K. Müller-Caspary, A. Rosenauer, and K. Volz, Influence of plasmon excitations on atomic-resolution quantitative 4D scanning transmission electron microscopy, *Sci. Rep.* **10**, 17890 (2020).
- [48] H. L. Robert, B. Diederichs, and K. Müller-Caspary, Contribution of multiple plasmon scattering in low-angle electron diffraction investigated by energy-filtered atomically resolved 4D-STEM, *Appl. Phys. Lett.* **121**, 213502 (2022).
- [49] J. Barthel, M. Cattaneo, B. G. Mendis, S. D. Findlay, and L. J. Allen, Angular dependence of fast-electron scattering from materials, *Phys. Rev. B* **101**, 184109 (2020).
- [50] L. Bian, J. Suo, J. Chung, X. Ou, C. Yang, F. Chen, and Q. Dai, Fourier ptychographic reconstruction using poisson maximum likelihood and truncated wirtinger gradient, *Sci. Rep.* **6**, 27384 (2016).